Published in Combustion and Flame https://doi.org/10.1016/j.combustflame.2022.112373

Effect of Lot Microstructure Variations on Detonation Performance of the Triaminotrinitrobenzene (TATB)-Based Insensitive High Explosive PBX 9502

Stephen J. Voelkel[a], Eric K. Anderson[a], Mark Short[a,*], Carlos Chiquete[a], Scott I. Jackson[a]

[a]*Los Alamos National Laboratory, Los Alamos, NM 87544, USA*

Abstract

PBX 9502 is an important insensitive high explosive due to its combination of safety properties and detonation performance levels. It is a polymer-bonded formulation consisting of 95 wt.% 1,3,5-triamino-2,4,6-trinitrobenzene (TATB) as the high explosive crystal, bound with Kel F-800 (FK-800), a co-polymer of chlorotrifluoroethylene and vinylidene-fluoride. Two different types are used, one known as virgin that uses only pristine manufactured TATB, and a second known as recycled that has 50 wt.% of its TATB reclaimed from machining scraps of previously pressed virgin PBX 9502. Recycled lots have a higher percentage of fine particles compared to virgin lots, due to the fracture and damage sustained by TATB crystals during pressing. We examine the influence that this TATB microstructure difference between virgin and recycled PBX 9502 has on detonation performance properties. New rate-stick geometry diameter effect, detonation front shape and cylinder expansion test data are obtained for two previously uncharacterized virgin lots and one recycled lot of PBX 9502. This is combined with legacy data for one virgin and one recycled lot for evaluation purposes. Detonation shock dynamics model calibrations are conducted on each of the five lots to provide an assessment of the detonation timing characteristics of virgin versus recycled PBX 9502 lots. For two of the virgin lots, detonations propagate slower in the rate-stick geometry than those in the two recycled lots. However, the other virgin lot tested has propagation rates comparable to that of the recycled lots. The latter result, though, is shown to be geometry dependent and depends on the range of detonation curvatures accessed in different geometries. New copper-confined, cylinder expansion tests are conducted on each of the three virgin and two recycled lots to obtain detonation product Jones-Wilkins-Lee equations of state, enabling an assessment of the metal push capabilities for each of the five lots. We find that the metal push capabilities, characterized by the evolution of the heat of detonation with volume, are similar between the virgin and recycled lots. Thus, changes in microstructure between different PBX 9502 lots seemingly affect the rate of reaction, but not the overall energy content.

Keywords:
Detonation, high explosive, PBX 9502, detonation shock dynamics, equations of state

1. Introduction

Insensitive high explosives (IHEs) are an important class of explosives for applications that necessitate a significant level of safety involving non-shock insults, but also require detonation performance properties approaching those of conventional high explosives. Examples of IHEs include PBX 9502 [1–3], LX-17 [4] and EDC35 [5, 6]. These polymer-bonded formulations use 1,3,5-triamino-2,4,6-trinitrobenzene (TATB) as the high explosive (HE) crystal, which are bound with Kel F-800 (FK-800), a co-polymer of chlorotrifluoroethylene and vinylidene-fluoride in a 3:1 ratio by weight [7]. PBX 9502 consists of 95 wt.% TATB with 5 wt.% Kel F-800 (FK-800), and is formed from molding powder pressed to a target density of 1.890±0.005 g/cm^3 [2]. The theoretical maximum density of PBX 9502 is 1.941 g/cm^3. It has a nominal Chapman-Jouguet (CJ) detonation speed of 7.8 mm/μs and a CJ pressure in the range of 28 GPa [3].

The TATB crystals are triclinic in shape, with a particle size distribution (PSD) range of $\sim$ 0.1 μm to $\sim$100 μm [8, 9]. The TATB crystals are fabricated through the Benziger process [10], whereby 1,3,5-trichlorobenzene is nitrated to yield 1,3,5-trichloro-2,4,6-trinitrobenzene

*Corresponding author:
Email address: short1@lanl.gov (Mark Short)

(TCTNB). The TCTNB is then dry-aminated to yield TATB. The conditions of the amination step are known to influence the TATB particle size distribution [9, 10]. PBX 9502 molding powder, consisting of an amalgamation of TATB particles coated in binder, is produced through a solvent-based lacquer process [10].

PBX 9502 has been in use as an IHE since the late 1970s and, subsequently, multiple batches of PBX 9502 molding powder have been manufactured. Each molding powder batch is assigned a designation known as a material lot. PBX 9502 molding powder that contains TATB produced directly from the Benziger process is called a virgin lot [2]. In contrast, recycled PBX 9502 lots have 50 wt.% of its TATB content recovered from machining scraps of pressed molding powder [2]. The pressing process is believed to significantly fracture and damage the TATB crystals and, consequently, PSD analysis shows that recycled lots generally have a higher percentage of fine particles compared to virgin lots [2, 9, 11]. Peterson and Idar [12] have also analyzed micrograph images of pressed pellets of virgin and recycled lots and showed that in the virgin lots coarse TATB crystals tended to agglomerate at various locations in the samples, whereas TATB crystals in the recycled samples were more evenly distributed. Such microstructure variations, although not well characterized, raise the potential of a detonation performance difference between virgin and recycled lots. This question is investigated in the current article.

Previously, Gustavsen et al. [2] studied PBX 9502 sustained-shock initiation characteristics between various virgin and recycled PBX 9502 lots by comparing the run-to-detonation distance for a range of shock-loading states. The authors were not able to identify any significant lot-to-lot differences. In contrast, Seitz [13] found that differences in TATB particle size distribution did significantly affect the initiation characteristics of PBX 9502 when subjected to short-duration-shock insults. Hill et al. [11] examined detonation performance timing variations between two virgin and two recycled PBX 9502 lots by comparing diameter effect and detonation shock shape differences. Using cubic curve fits through the diameter effect data, and an appeal to scaling arguments where insufficient data was available, Hill et al. [11] postulated that detonations in virgin lots propagated slower than in recycled lots. However, their analysis was limited by one of the virgin lots having data only at one diameter, and one of the recycled lots being a PBX 9502 development lot manufactured with a very high percentage of fine TATB particles [14], and also having no front shape data. Hill and Aslam [15] subsequently fitted a detonation shock dynamics (DSD) model to the lots examined in [11].

Importantly though, detonation performance assessments cannot be made with timing data alone. Timing is largely controlled by the multi-dimensional spatial structure of the detonation driving zone (DDZ) (the region between the detonation shock and sonic flow locus [16]), which depends significantly on the rate of reaction [3]. In addition, detonation performance assessments must also include both an evaluation of the energy content (heat of detonation) and an analysis of the capability of the explosive products to push a surrounding confiner, e.g. a metal, through an isentropic pressure release process such as in a cylinder test [17].

In the following, we describe several new detonation performance characterization rate-stick and cylinder tests on two virgin, newly formulated PBX 9502 lots (designations BAE18D755–001 and BAE20F755-002) and a recycled legacy PBX 9502 lot (HOL88B891–007). This data is then combined with legacy experimental rate-stick data for a virgin lot (HOL88H891–008) and a recycled lot (HOL85F000E–136) (both from [11]), augmented with new cylinder tests on both lots. Hereafter, we refer to lot designation BAE18D755–001 as 001-V, BAE20F755-002 as 002-V, HOL88B891–007 as 007-R, HOL88H891–008 as 008-V and HOL85F000E–136 as 136-R, where the V and R labels refer to virgin and recycled lots, respectively. Detonation shock dynamics model calibrations are conducted on each of the five lots, using both diameter-effect data and detonation front arrival-time data along a diameter chord of the charge. This provides the basis for an assessment of the detonation timing characteristics of recycled vs. virgin PBX 9502 lots. Detonation product Jones-Wilkins-Lee (JWL) equations of state (EOSs) are obtained from cylinder tests for lots 001-V, 002-V, 007-R, 008-V and 136-R to provide an assessment of their metal push capabilities.

For the rate-stick geometry, detonations in the virgin lots 002-V and 008-V propagate more slowly than for the recycled lots 007-R and 136-R across the range of diameters examined. However, interestingly, the speed of detonation in the virgin lot 001-V is comparable to that of the recycled lots 007-R and 136-R in the rate-stick geometry for larger diameters. For the two-dimensional circular arc geometry [3], where different regimes of curvature from the rate-stick geometry influence the detonation propagation rates, detonations in the three virgin lots 001-V, 002-V and 008-V are predicted to propagate slower than in the recycled lots 007-R and 136-R. Thus, the magnitude of the timing variation between lots is shown to be geometry dependent. We surmise that the timing difference between virgin and recy-

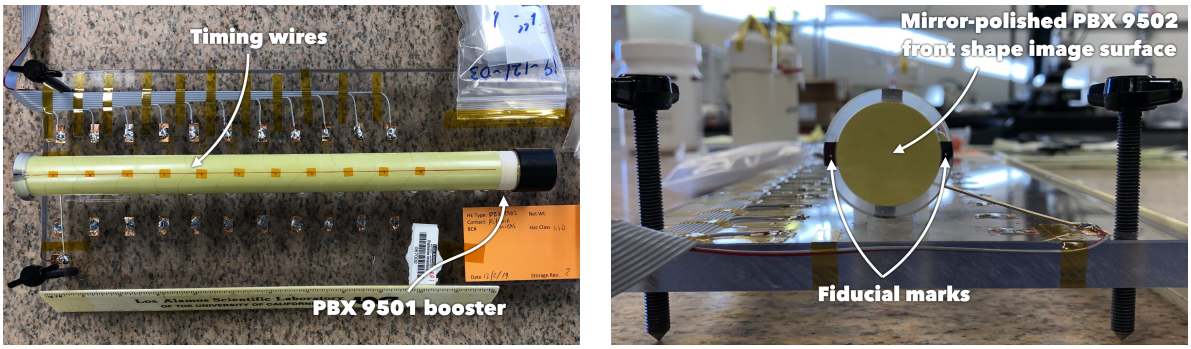

Figure 1: (Left) Rate-stick assembly for shot 8-2185 (lot 001-V). (Right) Outer ring fiducial for detonation shock arrival time measurements along a diameter chord at the end of the mirror polished charge for shot 8-2185.

cled lots is due to a slower rate of reaction in virgin lots associated with the larger TATB particle sizes, and the resulting effect this has on the amount of energy release that occurs within the DDZ [16] in any given geometry. In contrast, we find that the metal push capabilities and thus the overall energy content, characterized by the evolution in heat of detonation with volume, are similar between the virgin and recycled lots. Thus, changes in microstructure between different PBX 9502 lots seemingly affect the rate of reaction, but not the total energy content.

2. Experimental data for lot dependent PBX 9502

We have conducted four new unconfined rate-stick geometry experimental tests on the virgin lot 001-V (at diameters (d) of 12.70, 19.08, 25.36 and 50.83 mm), two on virgin lot 002-V (at diameters of 12.71 and 25.39 mm), and six on the recycled lot 007-R (at diameters of 12.71 − 12.72 (three tests), 19.06 (two tests) and 25.41 mm). The length of the PBX 9502 charge was $\approx 12d$ in all cases. For each test, we measured both the steady axial detonation speed (D_0) via ionization wire time-of-arrival (ToA) diagnostics, and the detonation front shape (more specifically, the arrival times of the detonation front along a diameter chord) using a mirror destruction technique imaged onto a streak camera, as shown in Fig. 1 [18, 19].

In addition to the timing and front shape data, we have also conducted five new cylinder expansion experiments (CYLEX) for lots 001-V, 002-V, 007-R, 008-V and 136-R. Each CYLEX test consisted of a nominal 25.4 mm diameter cylindrical HE charge, surrounded by a cylindrical copper (Cu) tube with a thickness of approximately one-tenth the HE charge diameter (Fig. 2). In the CYLEX test, as the detonation propagates axially, the detonation products expand, pushing the copper tube into a lateral motion. The radial velocity component of the Cu wall motion is then measured by Photon-Doppler-Velocimetry (PDV) diagnostics.

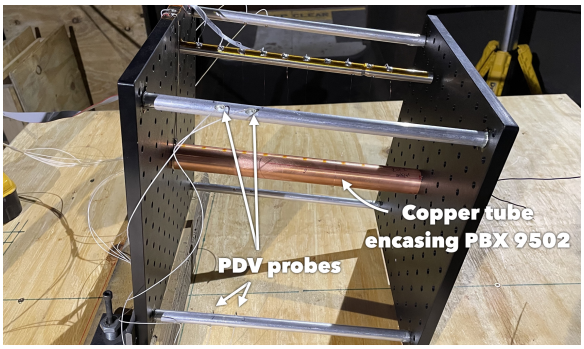

Figure 2: Cylinder test assembly for shot 8-2280 (lot 002-V). In addition to those shown, Photon-Doppler-Velocimetry (PDV) probes are also mounted on the opposite side of the assembly.

2.1. Rate-stick geometry tests

Dimensions and HE charge densities (ρ_0) for the lot 001-V, 002-V and 007-R rate-stick tests are given in tables 1–3. The HE cylindrical pellets (12 for each test) used to assemble the rate-stick tests were machined from isostatically pressed billets. The densities reported in tables 1–3 for lots 001-V, 002-V and 007-R represent averages of the pressed billets used for each test. Note that each pellet has a (immersion technique) density measurement accuracy of ±0.0005 g/cc. The standard deviation of the densities of the pellets used in each assembly is within the immersion measurement uncertainty of ±0.0005 g/cc. All tests were conducted at ambient conditions, nominally 25 °C. A linear least squares fit through the time-of-arrival data was used to obtain D_0 [18, 19] and is reported in tables 1–3 for lots 001-

Table 1: Rate-stick geometry data for virgin lot 001-V.

Shot Number	d (mm)	ρ_0 (g/cm^3)	D_0 (mm/μs)	Std. Error D_0 (m/s)
8-2188	50.83	1.895	7.679	0.44
8-2185	25.36	1.896	7.598	1.31
8-2186	19.08	1.895	7.555	1.59
8-2182	12.70	1.895	7.489	2.31

Table 2: Rate-stick geometry data for virgin lot 002-V.

Shot Number	d (mm)	ρ_0 (g/cm^3)	D_0 (mm/μs)	Std. Error D_0 (m/s)
8-2252	25.39	1.894	7.577	1.13
8-2251	12.71	1.890	7.472	2.73

Table 3: Rate-stick geometry data for recycled lot 007-R. The axial detonation speed on test 8-2017 was not obtained due to a failure with the time-of-arrival diagnostics.

Shot Number	d (mm)	ρ_0 (g/cm^3)	D_0 (mm/μs)	Std. Error D_0 (m/s)
8-2018	25.41	1.893	7.595	0.82
8-2020	19.06	1.894	7.566	0.77
8-2017	19.06	1.893	–	–
8-2019	12.71	1.893	7.492	2.32
8-2261	12.71	1.895	7.505	3.05
8-2284	12.72	1.896	7.505	2.15

Table 4: Rate-stick geometry data for virgin lot 008-V from [11]. The standard error on D_0 was not reported.

Shot Number	d (mm)	ρ_0 (g/cm^3)	D_0 (mm/μs)
15-2839	50.00	1.886	7.641
15-2529	18.01	1.886	7.523
15-2844	18.01	1.886	7.512
15-2851	10.01	1.890	7.421

Table 5: Rate-stick geometry data for recycled lot 136-R from [11]. Detonation front arrival times along a diameter chord for test C-6587 were not recorded, while the axial detonation speed for test 4-232 was not obtained. The standard error on D_0 was not reported.

Shot Number	d (mm)	ρ_0 (g/cm^3)	D_0 (mm/μs)
C-6589	50.02	1.895	7.677
4-232	50.00	1.892	–
C-6587	18.02	1.895	7.556
4-213	17.99	1.892	7.553
4-239	11.99	1.892	7.495
4-240	10.00	1.891	7.455
C-6588	9.99	1.895	7.457

V, 002-V and 007-R. The standard error of D_0 [20] associated with the linear fit is also shown. The successive arrival times of the detonation front along a diameter chord at the mirrored end of the charge were also recorded by streak camera imaging. Note that the arrival time data can be translated, if desired, into a detonation shock shape using the measured axial speed D_0 [18]. Previously published diameter effect data on virgin PBX 9502 lot 008-V (four tests) and recycled lot 136-R (seven tests) from [11] are shown in tables 4 and 5, respectively. Diameter chord arrival times were also obtained for the majority of the lot 008-V and 136-R tests. Information on density uncertainties for each of the lot 008-V and 136-R tests was not available.

The variation of D_0 with rate-stick charge size for all five PBX 9502 lots is shown in Fig. 3. The figure shows D_0 vs. $2/d$ (standard diameter effect plot) and D_0 vs. d. While the diameter effect variation will be discussed in detail in §3 in the context of virgin to recycled lot variability, it is worth noting for now that while the virgin lot 001-V and recycled lots 007-R and 136-R appear to have similar diameter effect variations (Fig. 3), D_0 for the virgin lots 002-V and 008-V is noticeably smaller than 001-V, 007-R and 136-R at comparable charge diameters by up to a few tens of meters per second.

Figure 4 shows a comparison of diameter chord arrival times in cases where there are comparable charge diameters for different lots. These are for $d = 50.0-50.8$ mm (lots 001-V, 008-V and 136-R), $d = 25.4$ mm (lots 001-V, 002-V and 007-R), $d = 18.0 - 19.1$ mm (lots 001-V, 007-R, 008-V and 136-R), $d = 12.0 - 12.7$ mm (lots 001-V, 002-V, 007-R and 136-R), and $d = 10.0$ mm (lots 008-V and 136-R). For the larger diameter charges ($d = 50.0 - 50.8$, $d = 25.4$ and $d = 18.0 - 19.1$ mm), the diameter chord arrival time fields are comparable between the virgin and recycled lots, while for the smaller diameter ranges ($d = 12.0 - 12.7$ and $d = 10.0$ mm), the diameter chord arrival times for the recycled lots 007-R and 136-R are broadly flatter than for the virgin lots 001-V, 002-V and 008-V.

2.2. CYLEX geometry tests

The dimensions of the five CYLEX tests on lots 001-V, 002-V, 007-R, 008-V and 136-R are shown in table 6. The five CYLEX tests were conducted at ambient conditions, nominally 25°C. The axial detonation speed and diameter chord arrival time fields were also recorded for each test. Eight collimated PDV probes were used to measure the motion of the Cu wall during each experiment. The PDV probes were oriented normal to the cylinder wall along a radial line prior to testing. Consequently, once the detonation pushes the Cu tube into a lateral motion, each PDV probe measures the radial velocity component of the Cu wall motion [17, 21]. Four PDV probes were located axially at $\approx$ 203.2 mm and four at $\approx$ 228.6 mm from the booster-PBX 9502 interface, corresponding to two-thirds and three-quarters of the total PBX 9502 charge length of each shot. At the two axial locations, each of the four probes was placed at a different azimuthal location, 90 degrees apart (Fig. 2).

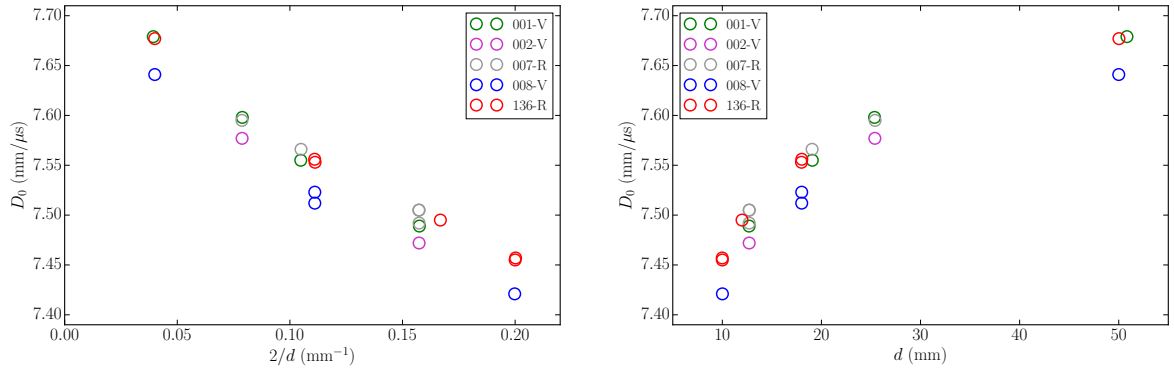

Figure 3: Diameter effect variation for lots 001-V, 002-V, 007-R, 008-V and 136-R.

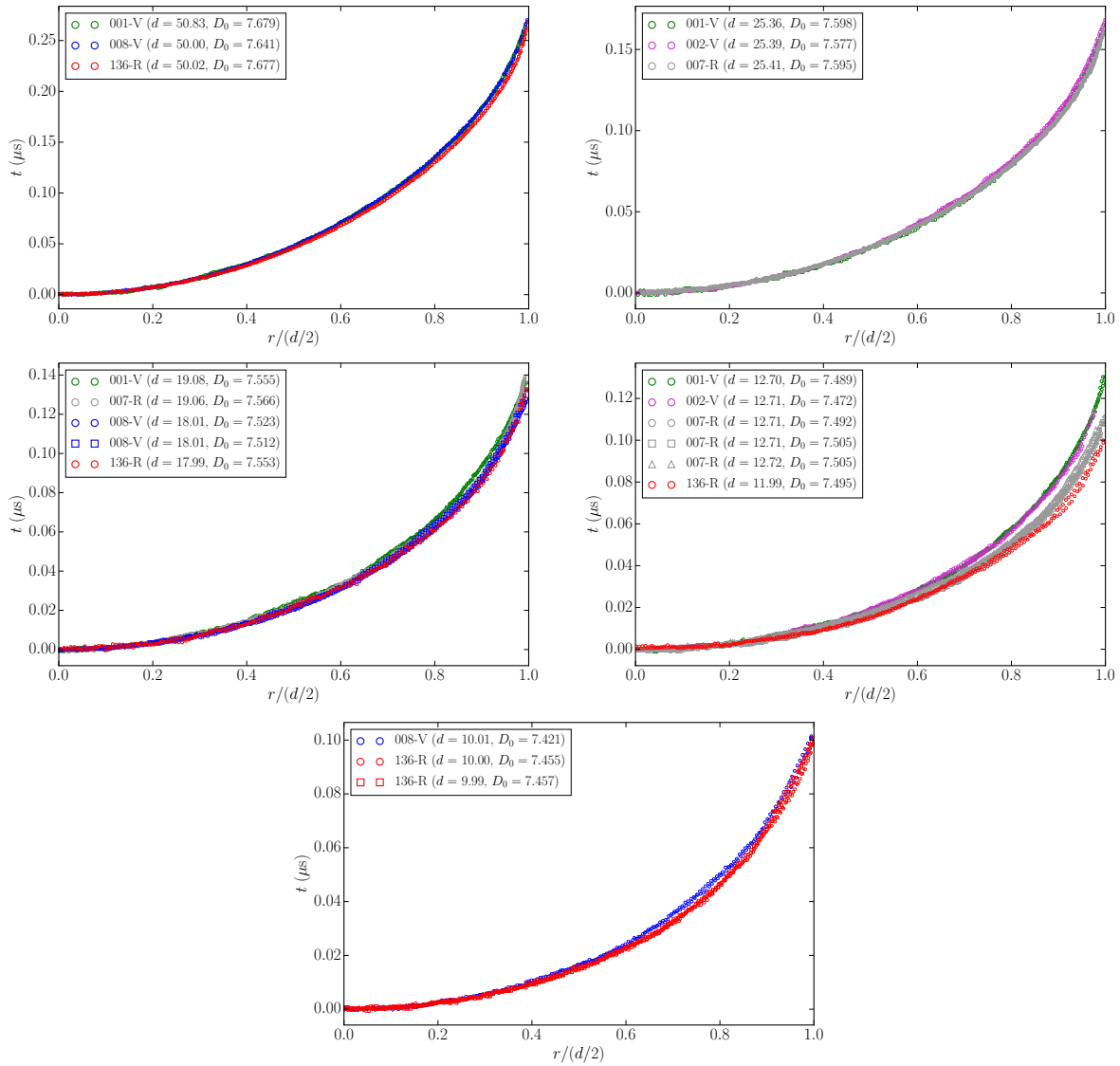

Figure 4: Comparison of diameter chord arrival time fields relative to the charge center between selected lots at comparable charge diameters. Diameters (d) are in mm, while axial detonation speeds D_0 are in mm/μs. Here r is the radial coordinate from the charge center ($r = 0$) to the charge edge ($r = d/2$). Note that for the purposes of presentation, arrival time data for $-d/2 \leq r \leq 0$ is reflected along the axial line $r = 0$ and shown with the arrival time data for $0 < r \leq d/2$, as described in [18].

Table 6: CYLEX geometry test data for lots 001-V, 002-V, 007-R, 008-V and 136-R. Here, Cu ID denotes the inner diameter, while Cu OD denotes the outer diameter of the copper tube. The length of the PBX 9502 charge was $\approx 12d$ in all cases.

Lot Number	Shot Number	d (mm)	Cu ID (mm)	Cu OD (mm)	ρ_0 (g/cm^3)	D_0 (mm/μs)	Std. Error D_0 (m/s)
001-V	8-2220	25.41	25.45	30.50	1.896	7.600	1.06
002-V	8-2280	25.39	25.43	30.50	1.895	7.589	1.51
007-R	8-2206	25.42	25.42	30.50	1.895	7.607	1.35
008-V	8-2205	25.43	25.44	30.49	1.891	7.582	1.79
136-R	8-2265	25.40	25.42	30.49	1.896	7.616	0.79

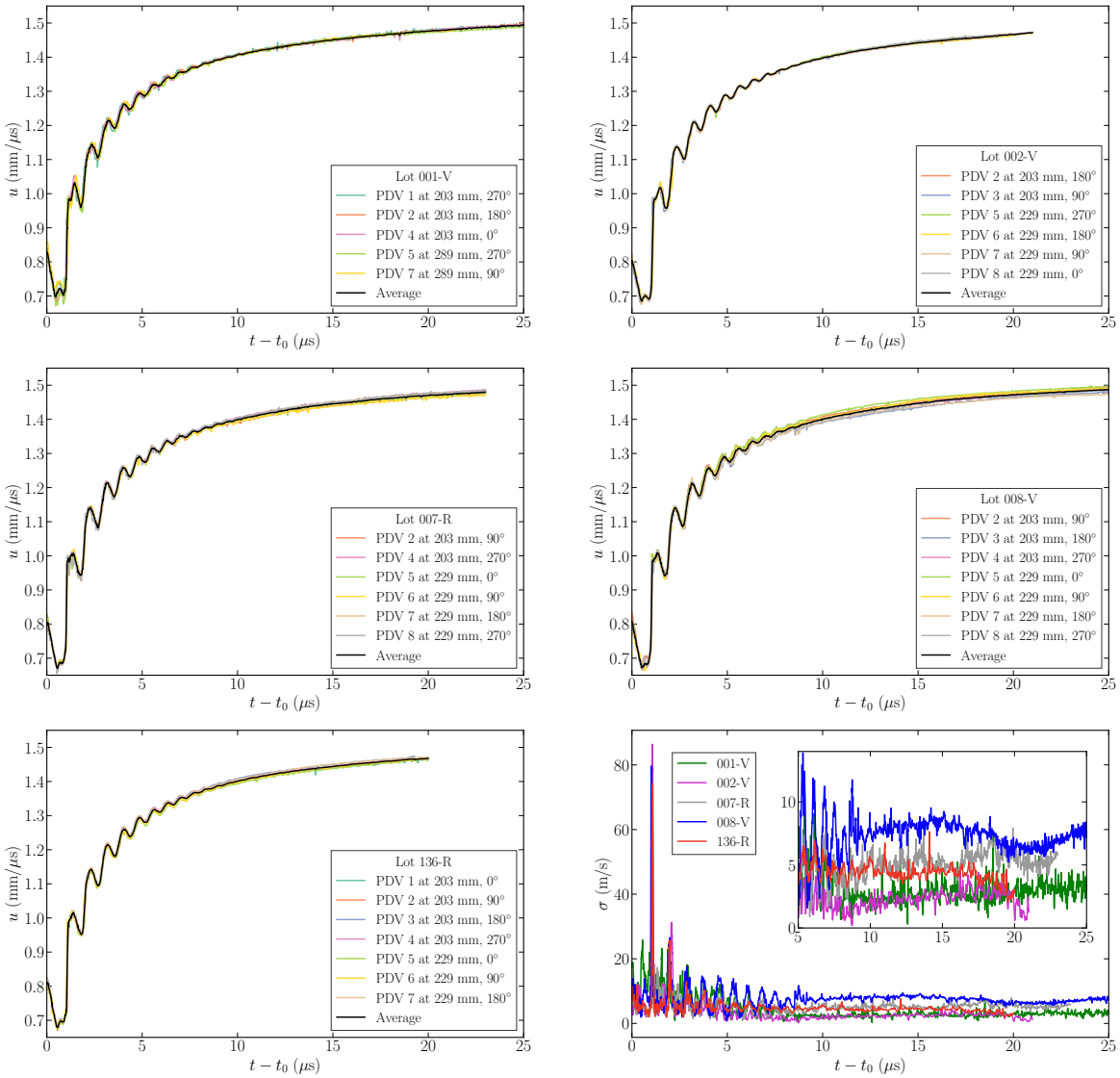

Figure 5: Measurement of the radial component of the outer Cu wall velocity (u) with time (t) relative to the time of wall motion start (t_0) for lots 001-V, 002-V, 007-R, 008-V and 136-R for the various PDV probe axial positions and angles shown. Also plotted for each lot are the velocity-time trace of the averaged PDV probe data. The bottom right figure shows the standard deviation of the PDV velocity traces from the average for each lot.

Figure 5 shows the PDV probe velocity histories in the radial direction of the Cu wall expansion for each of the CYLEX tests. A small number of PDV probes in each test either did not register a signal, or the signal

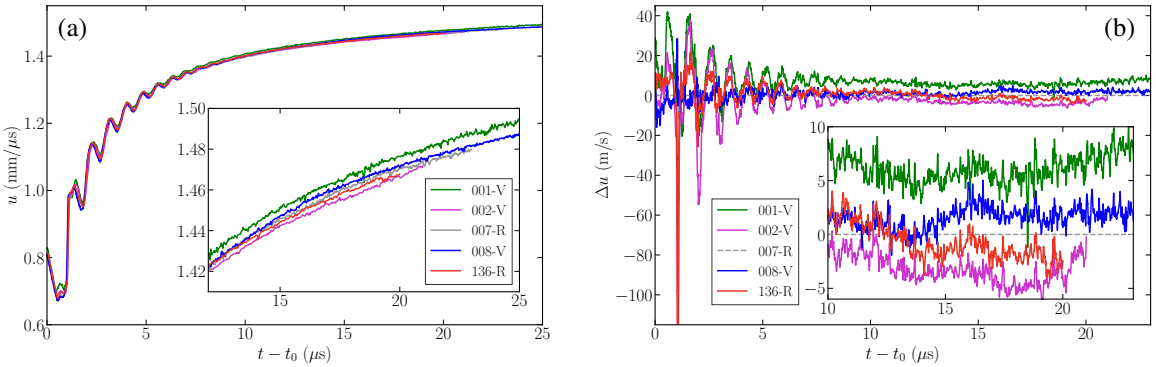

Figure 6: (a) Comparison of the averaged PDV traces for lots 001-V, 002-V, 007-R, 008-V and 136-R. (b) The difference in radial speed of the Cu wall motion for lots 001-V, 002-V, 008-V and 136-R relative to lot 007-R.

was weak, or the traces were statistical outliers, likely a result of the probes becoming misaligned to the Cu wall surface during shot preparation. The remaining PDV records are then aligned relative to the start of wall motion t_0 (Fig. 5). Each velocity history shows the presence of ringing in the early stages of the Cu tube push [17, 21], in which a combination of shocks, compressions or expansions reverberate within the Cu wall before dissipating at later times ($\approx$ 10 μs). At around 22-25 μs after wall motion start, the Cu tube starts to break apart and the PDV probe data terminates. Up to that point, for each lot, there is a moderately tight grouping of the PDV probe velocity histories.

The series of PDV probe velocity histories for each lot can be averaged by forming an arithmetic mean of the velocity histories at each $t - t_0$. These averages are also shown in Fig. 5. In addition, Fig. 5 shows the standard deviation of the velocity histories from the mean for each lot. The standard deviation is understandably higher in the ringing motion region, but becomes significantly smaller as the wall motion smooths, where the standard deviations are lower than 10 m/s (Fig. 5). Figure 6a shows a comparison of the averaged wall velocity histories for all lots. The averaged traces are very similar, with the speed differences of lots 001-V, 002-V, 008-V and 136-R relative to lot 007-R shown in Fig. 6b. Lot 001-V appears marginally higher in radial Cu wall speed relative to the other lots at late times (Fig. 6a), but the difference is close to the standard deviation of the other lots from their mean velocity histories (Fig. 5). Thus, to within experimental error, the Cu wall expansion histories for each lot are similar, despite lots 002-V and 008-V having slower detonation propagation speeds relative to lots 001-V, 007-R and 136-R (Fig. 3).

3. Detonation timing for lot dependent PBX 9502

A Detonation Shock Dynamics (DSD) detonation motion model for the PBX 9502 001-V, 002-V and 007-R lots was calibrated from the experimental diameter effect and diameter chord arrival time data. The DSD surface motion model assumes that the normal speed of the surface (D_n) at any point on the surface is a function of its local curvature (κ) [22]. The functional form of the D_n-κ relationship we used for each PBX 9502 lot is given by

$$D_n(\kappa) = D_{CJ}\left[1 - B\kappa\left(\frac{1 + C_2\kappa}{1 + C_4\kappa}\right)\right], \qquad (1)$$

where D_{CJ} is the CJ detonation velocity and B, C_2 and C_4 are function parameters to be calibrated, along with the angle ϕ_e between the DSD surface normal and the axial direction at the edge of the HE [18, 19]. A Nelder-Mead merit function minimization procedure [23] is used to fit the DSD model parameters to both the diameter effect and the diameter chord arrival time records for each lot. Additionally, corresponding DSD model calibrations based on previously published diameter effect and diameter chord arrival time data for lots 008-V and 136-R (tables 4 and 5) were obtained using the same merit function as for lots 001-V, 002-V and 007-R to prevent any fitting methodology biasing in the calibration between different lots.

Unlike the study in [15], we have not attempted to account for the potential effects of density variations within the PBX 9502 pressing tolerance range (1.890±0.005 g/cm^3) for any given lot due to a lack of statistically consistent data. For example, for lot 007-R, the two tests with d = 12.71 mm and ρ_0 = 1.893 and ρ_0 = 1.895 g/cm^3 have a D_0 difference of 13 m/s (table 3), comparable to the 11 m/s difference in D_0 for the

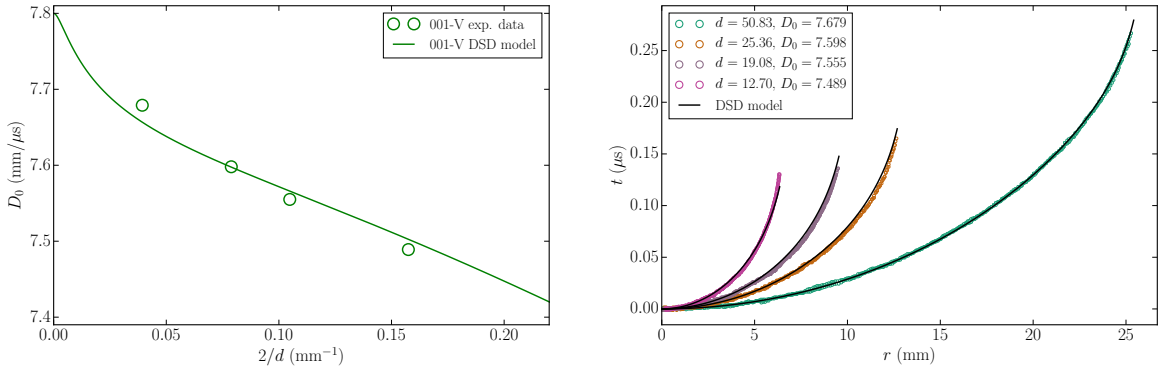

Figure 7: DSD model calibration of lot 001-V showing comparisons of the fitted diameter effect and the radial line (folded diameter chord) arrival time for each d with experimental data.

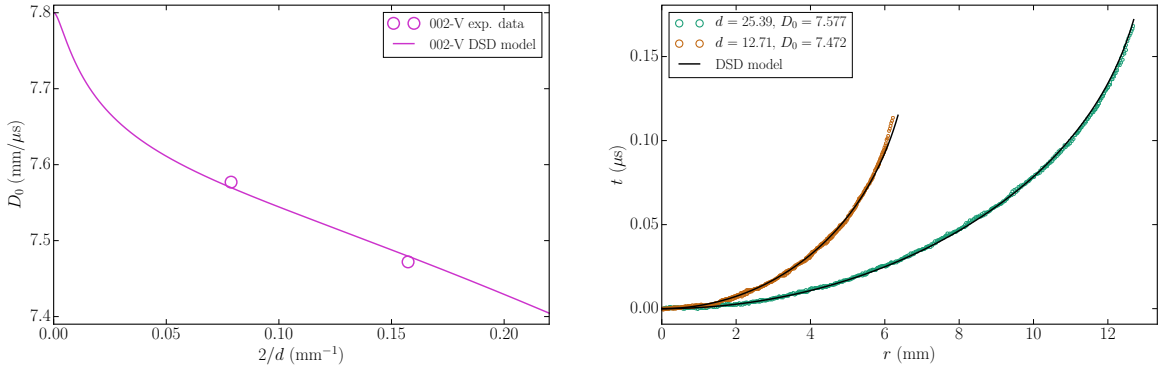

Figure 8: As for Fig. 7, but for lot 002-V.

two lot 008-V tests at d = 18.01 mm and ρ_0 = 1.886 g/cm^3 (table 4). Also, the two tests for lot 136-R at d = 18.0 mm and ρ_0 = 1.892 and ρ_0 = 1.895 g/cm^3 (table 5) result in D_0 values that differ by only 3 m/s, while the two tests at d = 10.0 mm with an even larger density difference (ρ_0 = 1.891 and ρ_0 = 1.895 g/cm^3) result in D_0 values that only differ by 2 m/s. Additionally, comparing lot 008-V at d = 10.01 mm and ρ_0 = 1.890 g/cm^3 (table 4) to lot 136-R at d = 10.00 mm and ρ_0 = 1.891 g/cm^3 (table 5), i.e. for a comparable density, shows that D_0 for lot 136-R is 34 m/s faster than that for lot 008-V. Given the nearly identical initial densities, the smaller D_0 obtained for lot 008-V cannot be attributed to density difference effects alone.

The DSD model fitting methodology used for each lot, as detailed in Appendix A, is a modification of that described in [18], and designed to provide an optimal balance between diameter effect and diameter chord (folded to a radial line) arrival time contributions, while accounting for repeat shots at similar diameters. Table 7 shows the lot 001-V, 002-V, 007-R, 008-V and 136-R optimized DSD model parameters based on the rate-stick geometry calibration process. The same global

Table 7: Lot 001-V, 002-V, 007-R, 008-V and 136-R DSD model parameters based on the rate-stick geometry calibration tests.

Lot Number	D_{CJ} (mm/μs)	ϕ_e (deg)	B (mm)	C_2 (mm)	C_4 (mm)
001-V	7.800	30.0	5.0318	8.6529	177.5389
002-V	7.800	30.0	5.9822	6.8219	180.1455
007-R	7.800	30.0	3.9395	5.0351	110.8340
008-V	7.800	30.0	6.5490	7.0329	199.4015
136-R	7.800	30.0	4.7489	7.3682	159.4875

values of D_{CJ} (7.8 mm/μs) and ϕ_e (30°) across all lots gave excellent fits for each individual lot (Appendix A). Moreover, the choice of a single value of D_{CJ} is consistent with the CYLEX analysis presented in §4, where the heats of detonation for the five PBX 9502 lots are found to be similar.

Figures 7–11 show the DSD model calibration fits of the diameter effect and radial line arrival times for each lot plotted with the corresponding lot-specific experimental data from §2. Figure 12 shows the difference in D_0 and the root-mean-square variation of the difference in diameter chord arrival times across the charge between the DSD model and experiment for each d and lot from Figs. 7–11. The calibration process has suc-

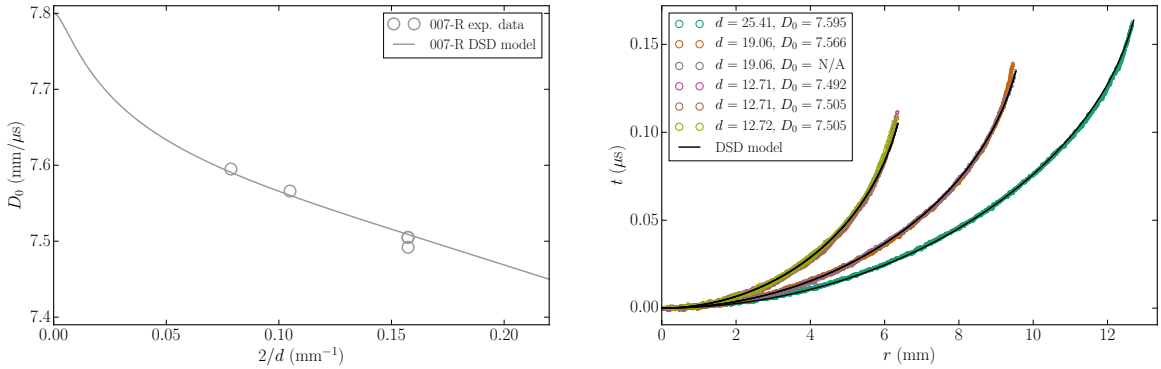

Figure 9: As for Fig. 7, but for lot 007-R.

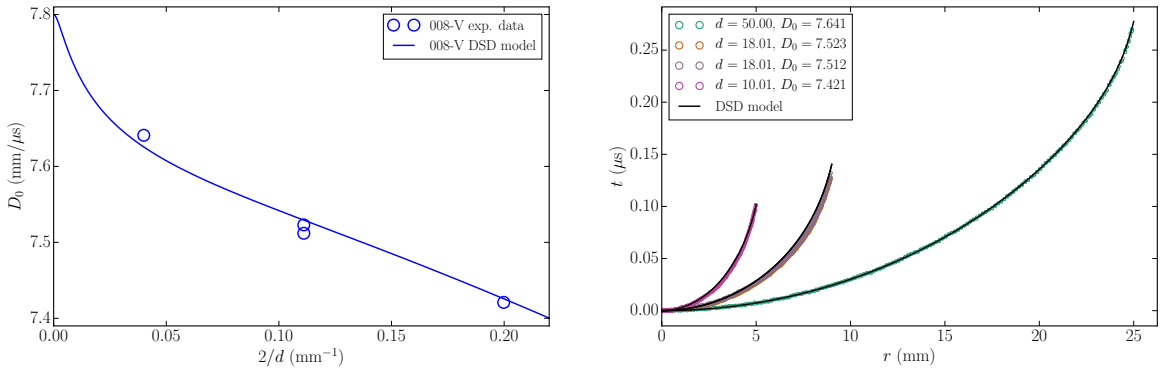

Figure 10: As for Fig. 7, but for lot 008-V.

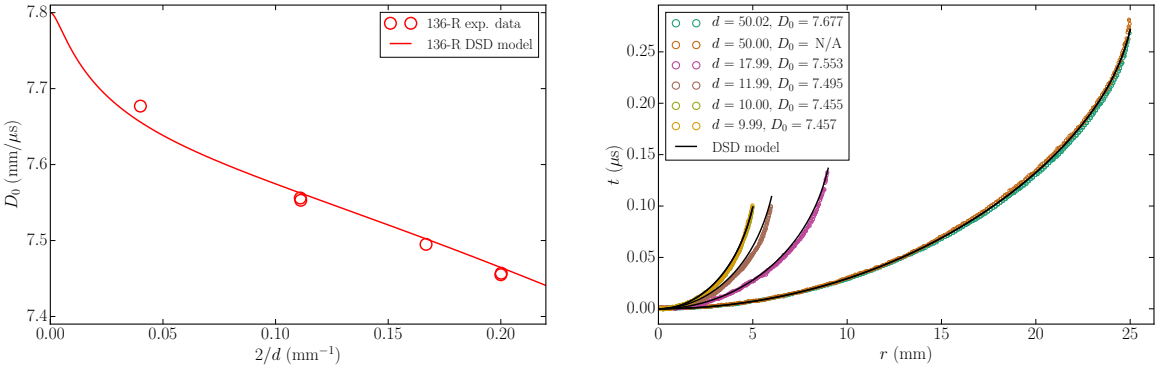

Figure 11: As for Fig. 7, but for lot 136-R.

cessfully achieved a balance between fitting the diameter effect and arrival time data for each lot.

Figure 13a shows the DSD model-based $D_n - \kappa$ variation between the five PBX 9502 lots. The variation between virgin and recycled lots is much less straightforward than that found in [11]. The main lot-to-lot differences are as follows. For $\kappa < 0.01$ mm^{-1}, the virgin lot 001-V and recycled lots 007-R and 136-R have similar D_n field variations, with D_n for lot 007-R marginally larger than for lots 001-V and 136-R. Between $0.01 < \kappa < 0.065$ mm^{-1}, the lot 007-R D_n field drops slightly below that of lots 001-V and 136-R, which maintain similar D_n variations. For $0.065 < \kappa < 0.1$ mm^{-1}, the D_n field for lot 001-V drops lower than that for lot 136-R, while the D_n field for lot 007-R moves up toward the lot 136-R field. The D_n field for lot 001-V crosses that for lot 007-R at $\kappa = 0.08$ mm^{-1}. For $\kappa > 0.1$ mm^{-1}, the recycled lot 007-R has significantly higher D_n values than for the recycled lot 136-R, which in turn has a D_n field that is now significantly larger than for the virgin lot 001-V. Meanwhile, the two virgin lots 002-V and 008-V have nearly coincident D_n fields that are slower

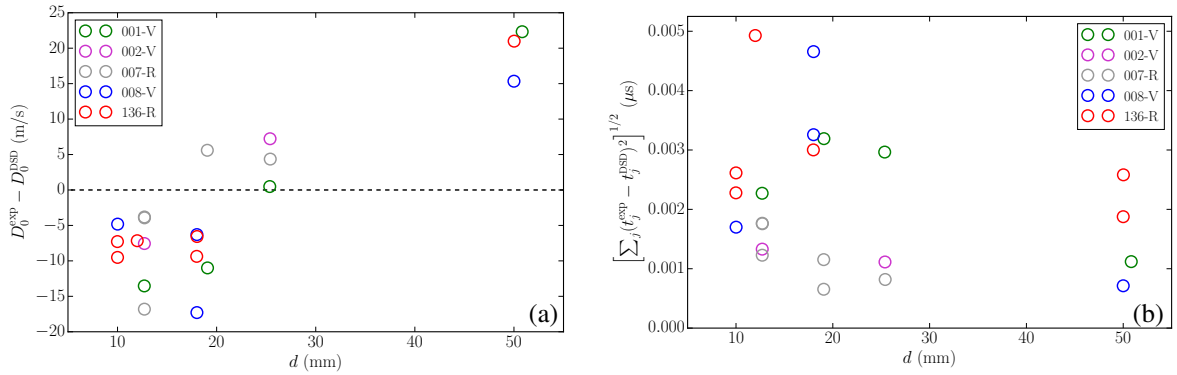

Figure 12: (a) Difference in axial detonation speeds $D_0^{\mathrm{exp}} - D_0^{\mathrm{DSD}}$ with charge diameter d between the experiment and DSD model for each lot. (b) Root-mean-square variation $[\sum_j (t_j^{\mathrm{exp}} - t_j^{\mathrm{DSD}})^2]^{1/2}$ of the difference in diameter chord arrival times across the charge for each diameter d between the experiment and DSD model for each lot.

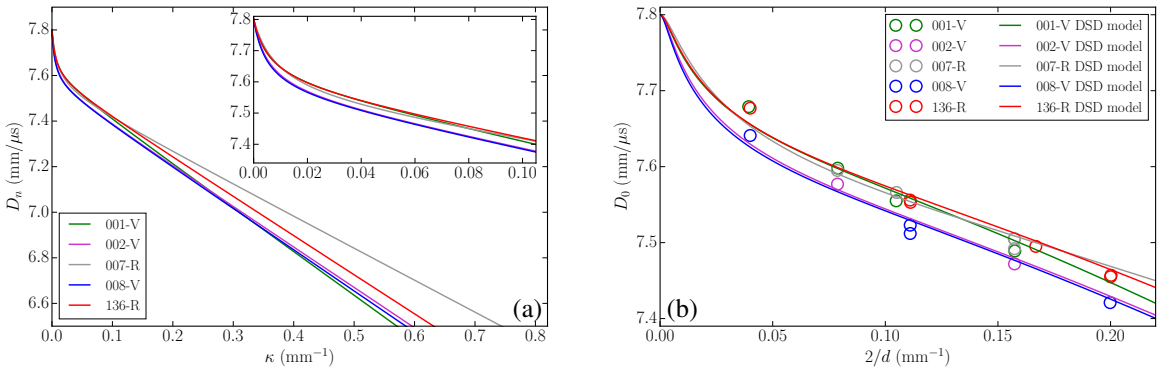

Figure 13: (a) $D_n - \kappa$ variation for lots 001-V, 002-V, 007-R, 008-V and 136-R derived from the fitted DSD models. (b) Diameter effect variation for lots 001-V, 002-V, 007-R, 008-V and 136-R showing comparisons of experimental data with the DSD models.

than that for both recycled lots 007-R and 136-R for all κ. This is despite the difference in densities between the lot 002-V and 008-V tests (tables 2 and 4). The D_n field for lot 001-V drops toward that of lots 002-V and 008-V in the range $0.065 < \kappa < 0.32$ mm^{-1} and becomes marginally slower than that for lots 002-V and 008-V for $\kappa > 0.32$ mm^{-1}.

In practice, only limited information can be gained on lot-specific detonation timing differences from knowledge of the $D_n - \kappa$ variations alone. Specifically, the detonation speed and arrival time record are determined by an integrated effect of the $D_n - \kappa$ variation (see Appendix A), and thus the range of curvatures accessed is strongly dependent on the nature of the HE geometry and is not known a priori. In this context, the fitted DSD model diameter effect curve for the five lots are shown in Fig. 13b. For $d > 57.0$ mm, the axial speeds D_0^{DSD} for lots 001-V, 007-R and 136-R are tightly grouped, with D_0^{DSD} for lot 007-R marginally above lots 001-V and 136-R. For 14.3 mm $< d <$ 57.0 mm, D_0^{DSD} for lot 007-R drops below that of lots 001-V and 136-R. Additionally, for $d < 22.2$ mm, D_0^{DSD} for lot 001-V drops below that of lot 136-R, and subsequently drops below that for lot 007-R for $d < 14.3$ mm. For $d < 11.1$ mm, D_0^{DSD} for lot 007-R increases above that for lot 136-R. Meanwhile, the DSD model diameter effect variation for lots 002-V and 008-V are very similar, and lie below those for lots 001-V, 007-R and 136-R. Overall, it is interesting that the virgin lot 001-V has a similar diameter effect variation to the two recycled lots 007-R and 136-R for larger diameters, while the virgin lots 002-V and 008-V trend slower than 001-V, 007-R and 136-R. This raises the question of whether the virgin lot 001-V is a potential outlier for PBX 9502 detonation timing effects at larger diameters, at least for the rate-stick geometry.

In order to gain additional insights into the diameter effect variation for lots 001-V, 002-V, 007-R, 008-V and 136-R, we can explore the D_n and κ field structure across the charge resulting from the integrated effect of the $D_n - \kappa$ coupling for different charge diameters. Figure 14 shows a comparison of DSD model surface shape (z_s) variations with radial coordinate r between lots 001-

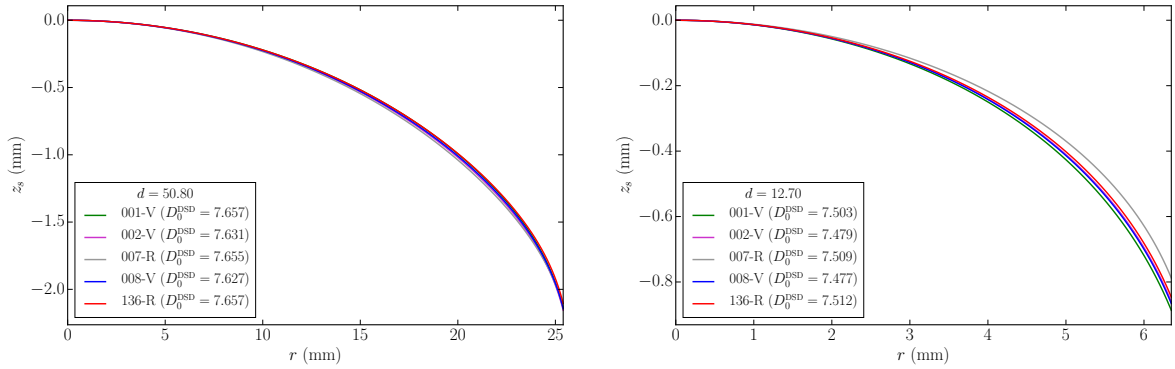

Figure 14: Comparison of DSD model surface shape variations z_s ($0 \le r \le d/2$) between lots 001-V, 002-V, 007-R, 008-V and 136-R at charge diameters of $d = 50.80$ mm and $d = 12.70$ mm.

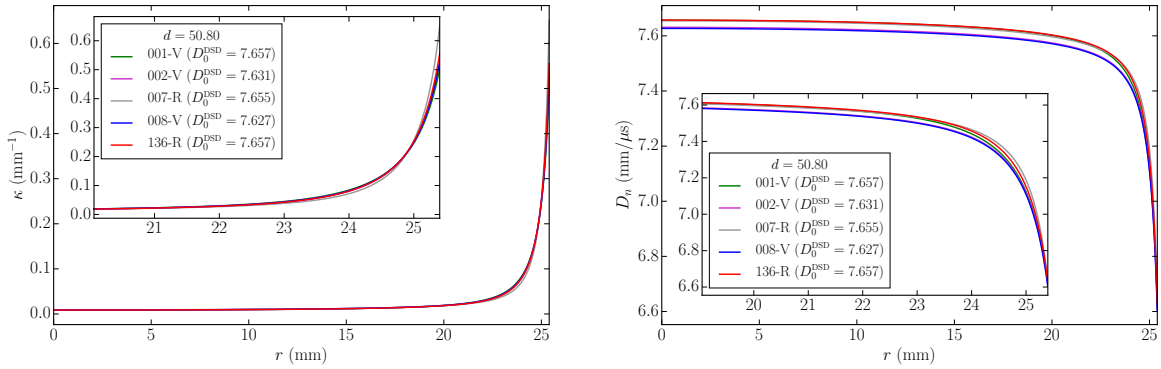

Figure 15: Comparison of curvature (κ) and normal surface speed (D_n) variations across the DSD model surface ($0 \le r \le d/2$) for lots 001-V, 002-V, 007-R, 008-V and 136-R with a charge diameter of $d = 50.80$ mm.

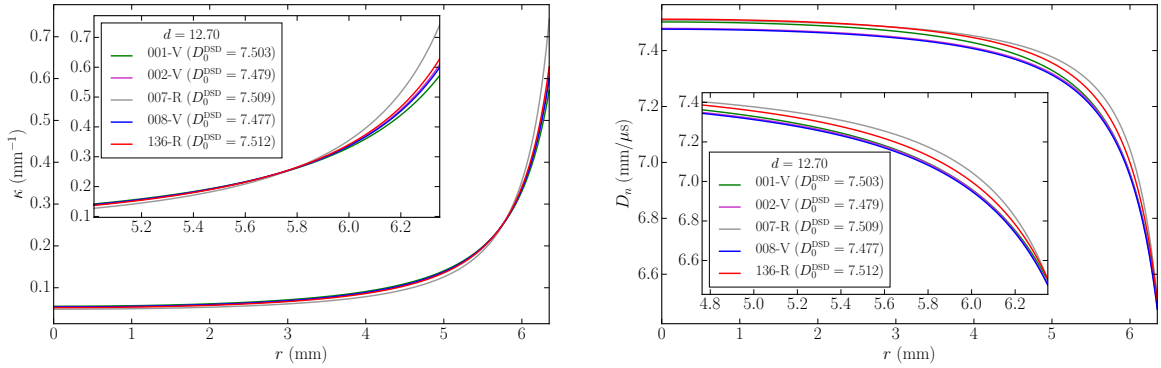

Figure 16: As for Fig. 15, but with $d = 12.70$ mm.

V, 002-V, 007-R, 008-V and 136-R at charge diameters of $d = 50.80$ mm and $d = 12.70$ mm, where $z_s(r)$ is related to the arrival time fields $t(r)$ by $t = -z_s/D_0$. The corresponding κ and D_n variations along the DSD surface for $d = 50.80$ mm and $d = 12.70$ mm are shown in Fig. 15 and Fig. 16, respectively. For $d = 50.80$ mm, the DSD surface shapes for all lots are similar across the charge radius. Correspondingly, the κ variations across the charge are very similar for each lot except at the charge edge (Fig. 15). The lot-to-lot relationship between κ and D_n (Fig. 13a) then determines the D_n variations across the $d = 50.80$ mm charge shown in Fig. 15. As expected, the D_n variations are similar for lots 001-V, 007-R and 136-R, but lower values of D_n are obtained for lots 002-V and 008-V, where the D_n fields for lots 002-V and 008-V are nearly coincident.

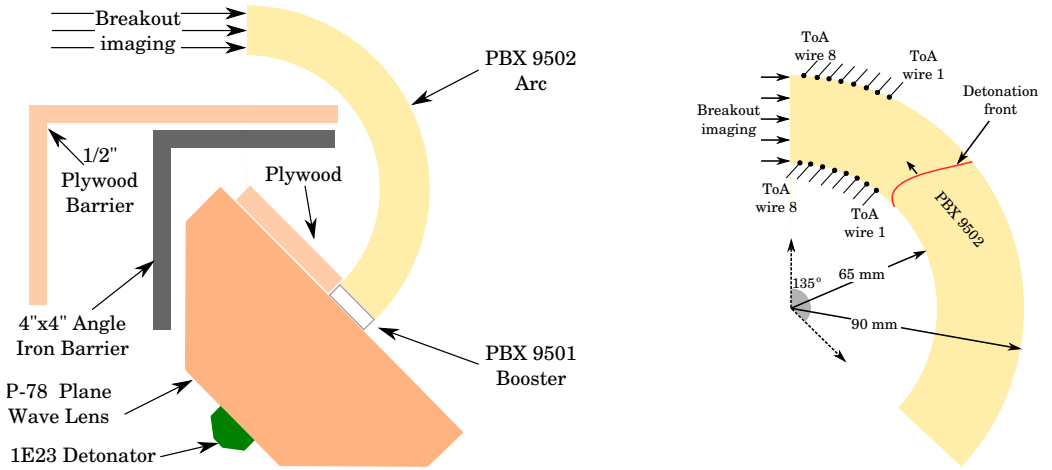

Figure 17: Schematics of the PBX 9502 lot 136-R 2D circular arc experiment showing the dimensions of the 2D plane section of the arc centerline. Both images are from [3].

The observed D_n behavior explains why the axial detonation speeds D_0^{DSD} are similar for lots 001-V, 007-R and 136-R, while D_0^{DSD} for lots 002-V and 008-V are about 30 m/s slower. Note that for the rate-stick geometry, regions of high curvature, where the D_n fields are more distinct between the lots (Fig. 15), are only obtained near the edge of the HE. In prior work, Jackson and Short [24] have shown that D_n variations near the edge do not affect D_0^{DSD} to leading order for large diameter charges, which is instead set by the interior D_n and κ variations.

For the smaller diameter charge of $d = 12.70$ mm (Fig. 14 and 16), the surface deflection z_s for lot 007-R is smaller than for lots 001-V, 002-V, 008-V and 136-R. Correspondingly, we observe a lower curvature for lot 007-R across the bulk of the charge than for the other lots (Fig. 16). At the charge center ($r = 0$), the κ magnitudes are such that with the $D_n - \kappa$ variation seen in Fig. 13a, D_n for lot 001-V is smaller than that for lots 007-R and 136-R, with D_n for lot 136-R slightly above that for lot 007-R. Moving away from the charge center, the D_n field for lots 007-R and 136-R evolve similarly, with D_n for lot 007-R moving above that for lot 136-R near the edge. This behavior is reflected in the close D_0^{DSD} values attained for these two lots, where $D_0^{\mathrm{DSD}} = 7.512$ mm/μs for lot 136-R, and $D_0^{\mathrm{DSD}} = 7.509$ mm/μs for lot 007-R. The D_n field for lot 001-V remains slightly smaller than both lots 007-R and 136-R across the charge, and $D_0^{\mathrm{DSD}} = 7.503$ mm/μs. As for $d = 50.80$ mm, the D_n field for lots 002-V and 008-V are very similar but lower than for lots 001-V, 007-R and 136-R across the charge, with $D_0^{\mathrm{DSD}} = 7.479$ mm/μs for lot 002-V and $D_0^{\mathrm{DSD}} = 7.477$ mm/μs for lot 008-V.

As noted above, the rate-stick geometry does not generally access the large curvature regimes away from the HE edge where the significant differences in the $D_n - \kappa$ profiles between the virgin 001-V, 002-V and 008-V and recycled 007-R and 136-R lots would influence the detonation propagation rates (Fig. 13a). In order to examine this effect, we study steady detonation propagation in a 2D circular arc configuration [3, 4, 18, 25–28]. Steady detonation propagation results after a relaxation process from the initiation event [25, 27]. In this geometry, Short et al. [25] showed that the steady detonation propagation mechanism is controlled by the curvature variations that occur in a small boundary layer attached to the inner arc surface, where regions of large detonation front curvature arise for unconfined arcs. A PBX 9502 lot 136-R arc experimental validation test was described in Short et al. [3] and consisted of a 64.98 mm inner radius (R_i) and 89.97 mm outer radius (R_e) arc (Fig. 17). The steady detonation speed on the inner ($r = R_i$) and outer ($r = R_e$) arc surfaces were measured (table 8), along with the detonation arrival time variation along a radial line from the inner ($r = R_i$) to outer ($r = R_e$) arc surface (Fig. 18).

Given the differences in D_n variations at large curvatures between the virgin 001-V, 002-V and 008-V and recycled 007-R and 136-R lots seen in Fig. 13a, we can use the PBX 9502 lot 136-R arc geometry test dimensions to predict the differences in the speed of the detonation sweeping around the arc for the five different lots. The DSD model can be used to model the 2D circular arc geometry as described in [18, 25], and leads to the linear speed predictions on $r = R_i$ and $r = R_e$ shown in table 8 for each lot. On $r = R_i$, both the re-

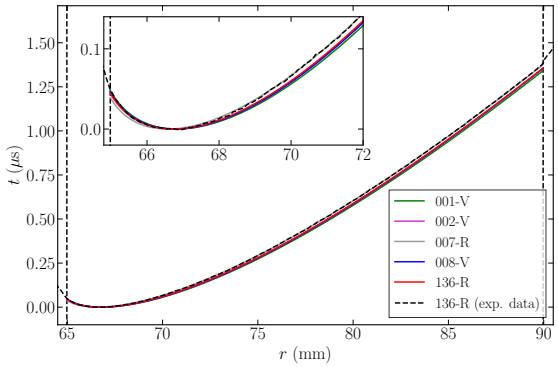

Figure 18: Comparison of lot 001-V, 002-V, 007-R, 008-V and 136-R DSD model arrival time variations along a radial line from the inner ($r = R_i$) to outer ($r = R_e$) arc surface. The experimental detonation arrival times [3] for lot 136-R are also shown.

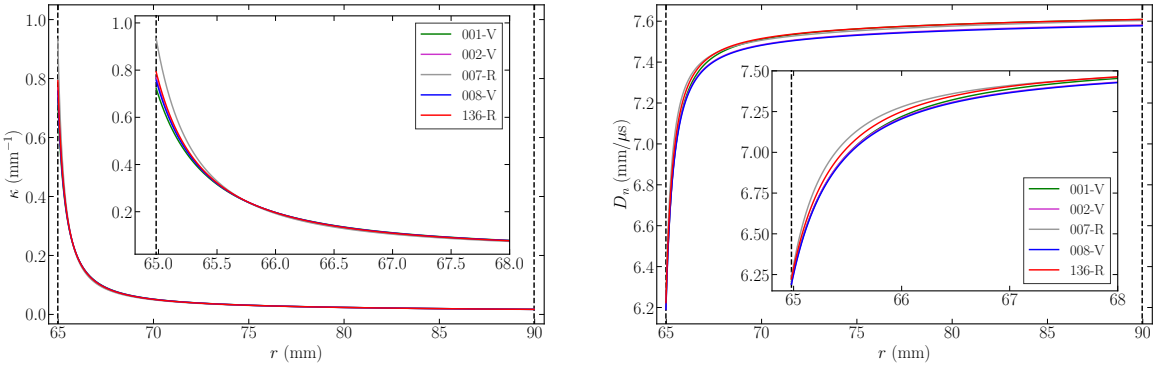

Figure 19: Comparison of curvature (κ) and normal surface speed (D_n) variations across the DSD model surface ($R_i \le r \le R_e$) for lots 001-V, 002-V, 007-R, 008-V and 136-R.

Table 8: DSD model prediction of the steady linear detonation speed on the inner ($r = R_i$) and outer ($r = R_e$) arc surfaces for lots 001-V, 002-V, 007-R, 008-V and 136-R. The equivalent speeds for the lot 136-R PBX 9502 experiment [3] are also shown.

	Linear speed on $r = R_i$ (mm/μs)	Linear Speed on $r = R_e$ (mm/μs)
Exp. (Lot 136-R)	7.155 (±0.027)	9.954 (±0.005)
Lot 008-V	7.146	9.894
Lot 002-V	7.150	9.899
Lot 001-V	7.166	9.922
Lot 136-R	7.184	9.947
Lot 007-R	7.196	9.963

cycled lots 007-R and 136-R are faster than the virgin lots 001-V, 002-V and 008-V, with the linear detonation speed in lot 007-R $\approx$ 50 m/s faster than in lots 002-V and 008-V. Also, the predicted speed in virgin lot 001-V lies midway between the recycled lot 136-R and virgin lots 002-V and 008-V. The radial line arrival time comparisons are shown in Fig. 18, while a comparison of curvature (κ) and normal surface speed (D_n) variations across the DSD model surface ($R_i \le r \le R_e$) for lots 001-V, 002-V, 007-R, 008-V and 136-R are shown in Fig 19. Most significantly, the D_n field variation for lots 007-R and 136-R in the boundary layer near $r = R_i$ is higher than for lots 001-V, 002-V and 008-V, with D_n for lot 007-R also higher than for lot 136-R, and D_n for lot 001-V slightly above that for lots 002-V and 008-V. It is this inner arc surface boundary layer variation that causes the detonation for recycled lots to sweep around the arc faster than for the virgin lots.

4. Detonation products metal push for lot dependent PBX 9502

As noted in §1, the CYLEX tests allow for the examination any lot-to-lot variation in push provided by the detonation products. In addition, these tests are used to calibrate a JWL product EOS for each of the 001-V, 002-V, 007-R, 008-V and 136-R lots examined. The JWL EOS is of Mie-Grüneisen form and is based on a reference curve describing the pressure (p_s) variation with volume (v) along the principal isentrope, i.e. that passing through the CJ point. The pressure along the

principal isentrope takes the form

$$p_s = A\exp[-R_1 v/v_0] + B\exp[-R_2 v/v_0] + C(v/v_0)^{-1-\omega}, \tag{2}$$

where C is a label parameter for the principal isentrope, v_0 (= $1/\rho_0$) is the initial specific volume of the HE, and A, R_1, B, R_2 and ω are the JWL EOS parameters, with $R_1 > R_2$. The JWL isentrope form (2) consists of two exponential functions, primarily active in high and moderate pressure regions, and an algebraic term that mimics an ideal gas form of isentropic variation for large volumes. The parameter ω is identified with Grüneisen gamma [29]. The associated specific internal energy variation along the principal isentrope is given by

$$\begin{aligned} e_s = \int_v^\infty p_s\, dv = \frac{Av_0}{R_1}\exp[-R_1 v/v_0] \\ + \frac{Bv_0}{R_2}\exp[-R_2 v/v_0] + \frac{Cv_0}{\omega}(v/v_0)^{-\omega}, \end{aligned} \tag{3}$$

with the reference point set so that $e_s \to 0$ as $v \to \infty$. For states off the principal isentrope, the Mie-Grüneisen EOS form is

$$p = p_s + \omega(e - e_s)/v, \tag{4}$$

or,

$$\begin{aligned} p = A\left(1 - \frac{\omega v_0}{R_1 v}\right)\exp[-R_1 v/v_0] \\ + B\left(1 - \frac{\omega v_0}{R_2 v}\right)\exp[-R_2 v/v_0] + \frac{\omega e}{v}. \end{aligned} \tag{5}$$

Note that the parameter C does not appear in this incomplete EOS form for pressure p and internal energy e.

The area under the isentrope from $v = v_{CJ}$ to $v = \infty$ minus the area under the Rayleigh line from $v = v_0$ to $v = v_{CJ}$ ($v_{CJ} < v_0$) defines the heat of detonation e_0, such that

$$e_0 = e_s(v_{CJ}) - p_{CJ}(v_0 - v_{CJ})/2, \tag{6}$$

and thus represents the total work that is done by the detonation products expanding along the principal isentrope [21]. The evolution in the detonation work with volume going from $v = v_{CJ}$ to v is given by $e_d(v) = e_0 - e_s(v) = e_s(v_{CJ}) - e_s(v) - p_{CJ}(v_0 - v_{CJ})/2$, so that $e_d(v_{CJ}) = -p_{CJ}(v_0 - v_{CJ})/2$ and $e_d(v \to \infty) = e_0$.

For each lot, we calibrate the JWL EOS model parameters A, B, R_1, R_2 and ω using a Nelder-Mead merit function minimization approach as described in Appendix B. Each CYLEX experiment is simulated in a Lagrangrian hydrocode [30] using a programmed burn (PB) simulation method for the HE. The DSD model for each specific lot in §3 is used for the HE PB timing component where, for the CYLEX experiments, the edge angles ϕ_e generated by the Cu confinement are calibrated by adjusting ϕ_e to fit the detonation front diameter chord arrival time variation measured in the CYLEX tests for lots 001-V, 002-V, 007-R, 008-V and 136-R (Fig. 20). The fitted DSD model edge angles are 18.2° (lot 001-V), 14.4° (lot 002-V), 13.1° (lot 007-R), 14.6° (008-V) and 14.6° (136-R). The corresponding HE PB energy release component is calculated through a velocity-adjusted JWL method [6, 18, 19, 31]. This accounts for the influence of detonation front curvature on the evolution of the detonation products, an effect normally neglected in the calibration of HE detonation product equations of state. The details of the velocity-adjusted JWL methodology as utilized in the current study are described in Appendix C. The Cu confiner in the simulations is modeled with a tabular EOS [32], together with the plastic deformation model and its Cu parameterization defined in [33]. The starting mesh resolution was 62.5 μm based on a uniform grid. The aspect ratio of the CYLEX computations was 8.

The simulated and experimentally measured Cu wall radial expansion profiles, i.e. the averaged PDV profiles shown in Fig. 6a, are compared and A, B, R_1, R_2 and ω then iterated on to provide the desired level of fit (Appendix B). A recent validation study [34] of this JWL EOS calibration methodology describes how, when a JWL product EOS is calibrated to a Cu wall expansion CYLEX geometry test as described above, the derived EOS accurately predicts the lateral motion, separately, of a copper and tantalum plate in a confined 2D planar slab geometry. Table 9 shows the final JWL product EOS parameters A, B, R_1, R_2 and ω obtained from the minimization process for each of the 001-V, 002-V, 007-R, 008-V and 136-R lots, along with the corresponding heat of detonation e_0.

Figure 21 shows a comparison of the averaged experimental PDV probe radial velocity fields (from Fig. 6a) with the simulated wall motions based on the final calibrated JWL EOS model for each lot (table 9). The relative velocity differences between the experiment and fitted JWL EOS model simulation for each lot is also shown in Fig. 21. The simulations with the calibrated JWL detonation products EOSs are able to capture the experimental data well, with small errors in the smooth regions of the wall expansion. Figure 22 shows a comparison of the radial wall speeds based on the simulations with the JWL EOS models across the five lots. Due to the successful fitting process, the trends between

Table 9: JWL product EOS parameters for lots 001-V, 002-V, 007-R, 008-V and 136-R.

Lot Number	A (GPa)	B (GPa)	R_1	R_2	ω	ρ_0 (g/cm^3)	$e_d(v = 1.5)$ (mm^2/μs^2)	$e_d(v = 4.5)$ (mm^2/μs^2)	$e_d(v = 7.5)$ (mm^2/μs^2)	e_0 (mm^2/μs^2)
001-V	696.6707	16.7105	4.5676	1.6502	0.3316	1.8950	2.7791	3.1369	3.2463	3.8390
002-V	705.1466	17.4491	4.5882	1.6648	0.3153	1.8950	2.7655	3.1124	3.2194	3.8323
007-R	697.9858	17.1349	4.5724	1.6600	0.3177	1.8950	2.7753	3.1294	3.2390	3.8605
008-V	701.7002	17.0674	4.5777	1.6652	0.3186	1.8950	2.7625	3.1169	3.2267	3.8483
136-R	711.0371	17.0673	4.5984	1.6312	0.3188	1.8950	2.7799	3.1221	3.2255	3.8103

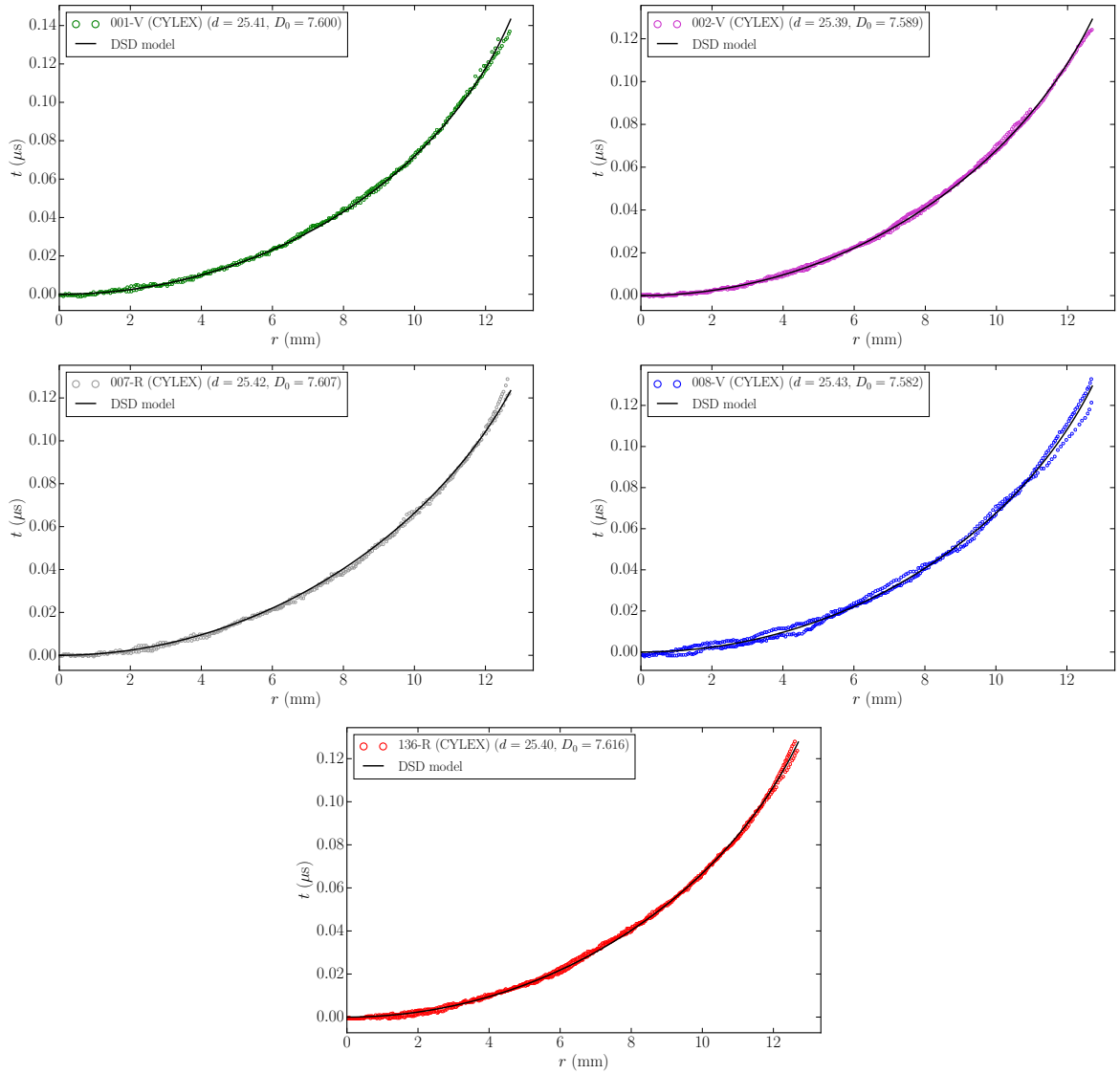

Figure 20: Detonation front diameter chord (radial line) arrival times for the DSD model after calibrating the DSD model edge angles ϕ_e with the experimentally measured lot 001-V, 002-V, 007-R, 008-V and 136-R arrival times in the CYLEX tests.

lots in the simulated radial wall speed evolution are similar to those described in the experimental observations seen in Fig. 6a, with lot 001-V appearing marginally higher in radial Cu wall speed relative to lots 007-R and 008-V at late times, which in turn are marginally higher than for lots 002-V and 136-R, but with the differences in wall velocity at late times close to the standard deviation of all the lots from their mean experimental velocity

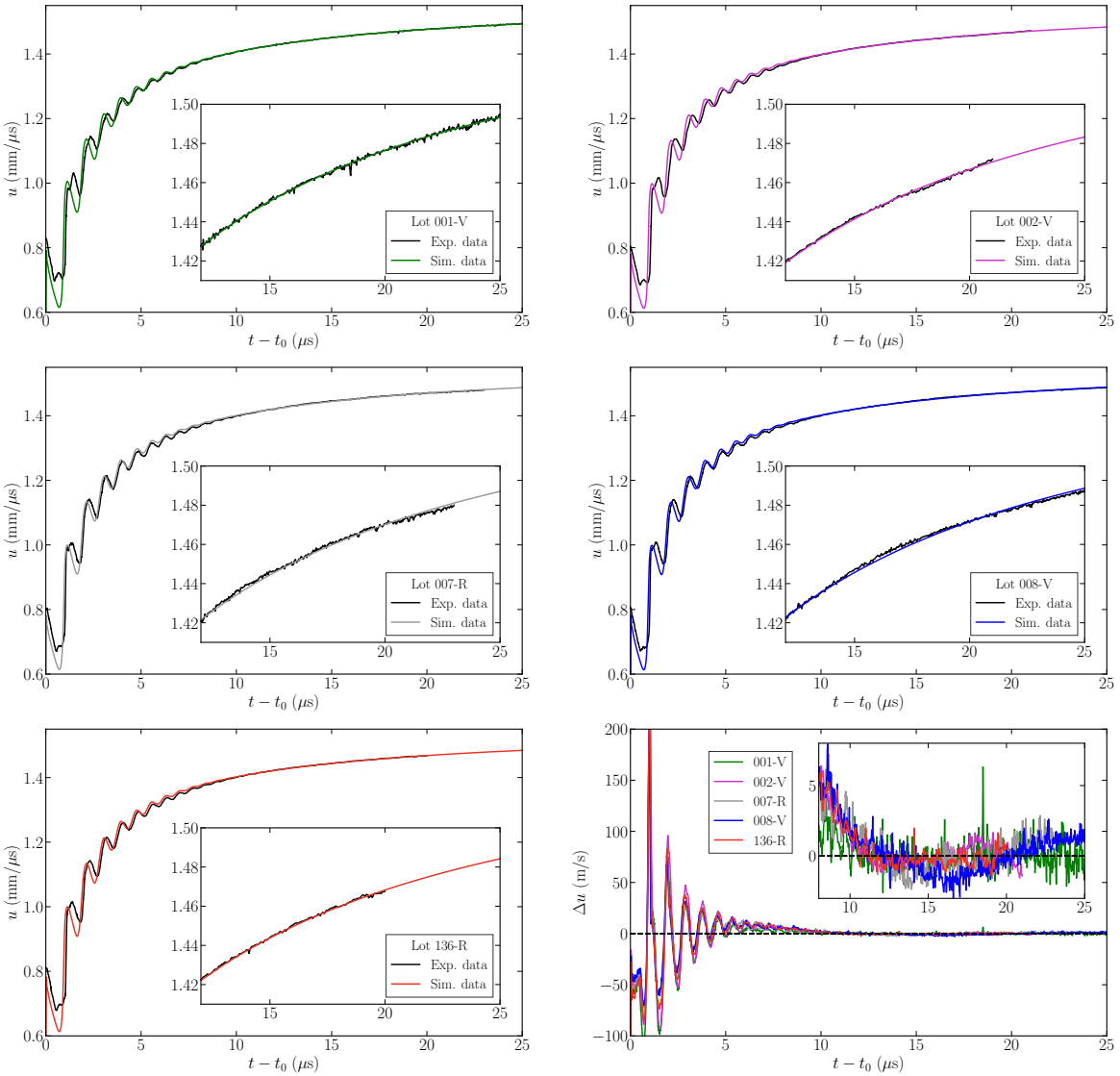

Figure 21: Comparison of the averaged PDV probe radial velocity field (Fig. 6a) with the simulated wall motion based on the calibrated JWL EOS model for each lot (table 9). The bottom right plot shows the corresponding difference Δu in the simulation and experimental Cu wall radial velocity for each lot.

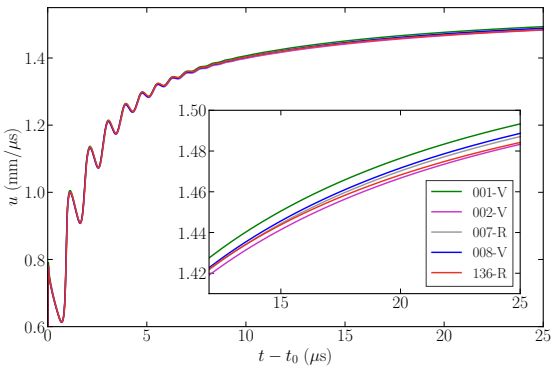

Figure 22: A comparison of the CYLEX radial wall motion simulations between the five lots.

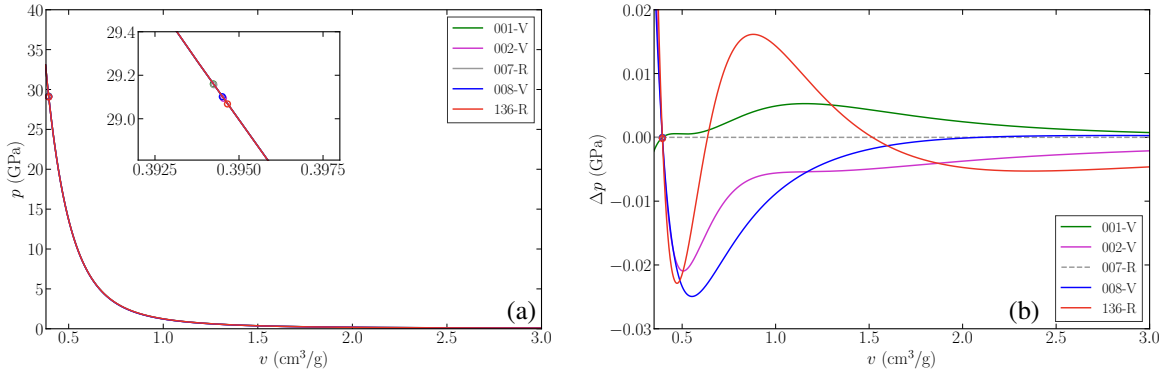

Figure 23: (a) Comparison of the JWL principal isentropes for lots 001-V, 002-V, 007-R, 008-V and 136-R up to $v = 3$ cm^3/g. (b) Lot 001-V, 002-V, 008-V and 136-R pressure difference (Δp) along their principal isentropes relative to lot 007-R. The circles indicate the CJ state for each lot.

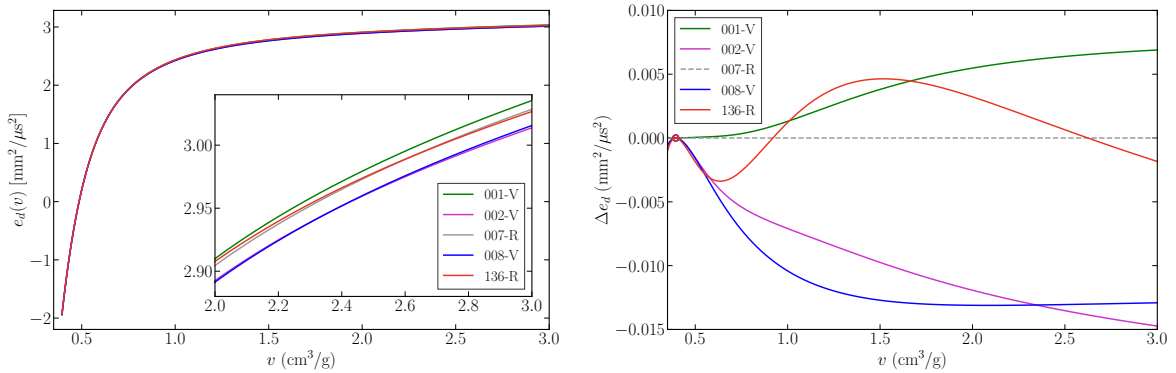

Figure 24: Detonation product work variation $e_d(v) = e_0 - e_s(v)$ for each lot and the difference in e_d (Δe_d) for lots 001-V, 002-V, 008-V and 136-R relative to lot 007-R up to $v = 3$ cm^3/g.

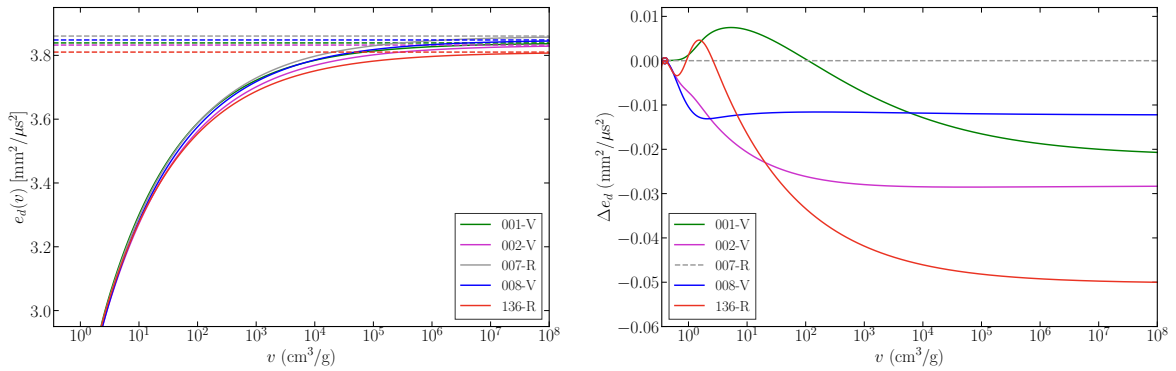

Figure 25: As for Fig. 24, but for large v. The dashed lines in the plot for $e_d(v)$ indicate the values of the heat of detonation e_0 for each lot.

histories (Fig 5).

The principal isentrope variation for lots 001-V, 002-V, 007-R, 008-V and 136-R derived from the JWL product EOSs is shown in Fig. 23a for volumes v up to $v = 3$ cm^3/g, with the isentrope pressure differences of lots 001-V, 002-V, 008-V and 136-R relative to lot 007-R shown in Fig. 23b. The CJ pressure for both lots 001-V and 007-R is marginally larger than that for lots 002-V, 008-V and 136-R, while the CJ volume for lots 001-V and 007-R is slightly lower than for lots 002-V, 008-V and 136-R. Thus, lots 001-V and 007-R are marginally more compressed at the CJ state. Significantly, however, there are no major quantitative differences in the CJ isentrope pressure variation with volume between

the five lots (Fig. 23a,b). For most of the isentrope pressure variations with volume, the pressure differences between the lots is within 0.02 GPa.

The corresponding variation in the detonation product work e_d with volume, together with the differences in e_d for lots 001-V, 002-V, 008-V and 136-R relative to lot 007-R, are shown in Fig. 24 and Fig. 25 for two different volume scales. The most significant data is the detonation product work variation $e_d(v)$ up to $v \approx 7.5$ cm^3/g. From our CYLEX simulations, this is calculated to be the HE volume reached along the HE/Cu interface at which the Cu walls in the CYLEX experiments begin to disintegrate. Table 9 gives specific values of $e_d(v)$ for $v = 1.5$, 4.5 and 7.5 cm^3/g for each lot, where the corresponding pressure along the CJ isentropes are $p_s \approx 0.1$, 0.07 and 0.05 GPa, respectively. Additionally, for each lot, at $v = 1.5$ cm^3/g, $e_d \approx 72\%$ of e_0, at $v = 4.5$ cm^3/g, $e_d \approx 82\%$ of e_0, and at $v = 7.5$ cm^3/g, $e_d \approx 85\%$ of e_0. Up to $v \approx 7.5$ cm^3/g, the detonation work provided by the five lots are close (Fig. 24 and table 9). Only when the products have expanded to very large volumes, several magnitudes higher than v_{CJ}, does the total detonation work approach the heat of detonation e_0 (Fig. 25). The heat of detonation for lot 007-R is larger than for lots 001-V, 002-V and 008-V, which are higher than for lot 136-R (table 9). However, it also clear that the heat of detonation is influenced significantly by the contributions of very small CJ isentrope pressures integrated over very large volumes (Fig. 25). For this reason, e_0 is not an insightful indicator of the detonation product work difference between the five lots. Rather, $e_d(v \approx 7.5$ cm^3/g) is a more relevant indicator of the useful detonation work for the reasons described above. Thus, based on an analysis of both the cylinder tests and JWL product EOSs, we conclude that the metal push capabilities, characterized by the evolution in detonation work with volume, are therefore similar for each of the five lots, i.e. for the three virgin and two recycled lots.

5. Summary

We have examined detonation performance characteristics of virgin and recycled lots of the 1,3,5-triamino-2,4,6-trinitrobenzene (TATB)-based insensitive high explosive PBX 9502. Both types of lots are manufactured in a nominally identical way, except recycled PBX 9502 lots have 50 wt.% of its TATB content recovered from machining scraps of pressed molding powder, and therefore contain a higher percentage of fractured and damaged TATB crystals relative to virgin lots. New rate-stick geometry diameter effect data, detonation front time-of-arrival data along a diameter chord, and cylinder expansion (CYLEX) data are obtained for two previously uncharacterized virgin PBX 9502 lots and one recycled PBX 9502 lots. This is combined with legacy timing and shape data for one additional virgin and one additional recycled PBX 9502 lot, along with new CYLEX data for both lots.

Detonation shock dynamics model calibrations are conducted on each of the five lots to provide an assessment of the detonation timing characteristics of virgin versus recycled PBX 9502, while detonation product Jones-Wilkins-Lee (JWL) equations of state (EOS) are also obtained for the five lots to provide an assessment of the metal push capabilities of the virgin and recycled lots.

We found that for two of the virgin lots, detonations propagate slower in the rate-stick geometry than those in the two recycled lots. However, interestingly, the other virgin lot tested has propagation rates comparable to that of the recycled lots for larger diameter tests. The timing effect, though, is shown to be geometry dependent and depends on the range of detonation curvatures accessed in different geometries. In a 2D circular arc geometry, for instance, we predicted that detonations in the three virgin lots will sweep around the arc more slowly than those in the two recycled lots. In contrast, based on the results of the JWL product EOS calibration, we concluded that the metal push capabilities, characterized by the evolution in detonation products work with volume, between the virgin and recycled lots are very similar.

In summary, for steady waves, the PBX 9502 detonation speed is influenced by the energy release that occurs within the DDZ [16], i.e. the region of flow contained within the detonation shock and sonic locus. Depending on the geometry, and which ranges of curvature are therefore accessed, we conjecture that virgin lots broadly have slower kinetics relative to recycled lots, resulting in a slower rate of energy release in the DDZ, and hence slower propagation rates. It is plausible that this behavior is related to the higher percentage of fine TATB particles in recycled lots than virgin lots [2, 9, 11, 12]. However, the overall energy content of the various lots are similar, an important result for high explosive applications.

In future work, we will pursue the challenging problem of the development and comparison of techniques to accurately measure the TATB particle size distributions (PSDs) in virgin and recycled lots of PBX 9502 for the pressed material. In light of the above observations, there is no guarantee, for example, that lot 001-V has a similar PSD to lots 002-V and 008-V, even though they are all virgin lots. Ideally, we would like to have a de-

tailed PSD analysis for each of the virgin and recycled lots studied here to further explore this behavior, one that extends beyond the limited studies that have shown recycled lots generally have more fine TATB particles than virgin lots [2, 9, 11, 12]. However, this is a very challenging problem. One major issue is that the TATB particles are triclinic in shape, and therefore common sieving methodologies are limited. The second is that we would like the PSD to be conducted on the pressed material [11], where it is believed significant damage to the TATB crystals is induced by the pressing process. In order for that analysis to occur, a solvent process will need to be utilized to cleanly strip the binder from the pressed pellets of PBX 9502, so that the binder does not affect TATB PSD analysis. Comparisons must then be made between different PSD techniques, such as sieving, laser diffraction, and framing camera imaging.

In addition, we are currently assessing the effect of lot dependency on the PBX 9502 detonation failure diameter. Identification of the precise failure diameter is challenging experimentally, as failure occurs very abruptly once the rate-stick failure diameter is reached.

In closing, we note that many common high explosives (HEs) have been continuously manufactured and used for many decades. As manufacturing processes change, the size and nature of the HE crystal distributions are affected. This is the first study to systematically examine the lot-to-lot detonation performance of any HE that involves both an evaluation of its timing and metal push properties.

Appendix A. DSD Model Calibration Methodology

The DSD model predicted detonation axial speed and diameter chord arrival time for a given rate-stick diameter d is determined through the solution of

$$\frac{dr}{d\phi} = \frac{\cos\phi}{\kappa_s},\ \frac{dz_s}{d\phi} = -\frac{\sin\phi}{\kappa_s},$$
$$z_s(\phi = 0) = 0,\ r(\phi = 0) = 0,\ r(\phi = \phi_e) = d/2, \tag{A.1}$$

where r is the radial coordinate ($0 \le r \le d/2$), ϕ is the angle between the axial direction of the rate-stick and the surface normal at any point on the DSD surface, $\kappa_s = d\phi/d\xi$ is the slab component of the total curvature, where ξ is the surface arclength, and z_s is the shape of the DSD surface. Additionally,

$$D_n = D_0^{\mathrm{DSD}}\cos\phi,\ \kappa_s = \kappa - \frac{\sin\phi}{r}, \tag{A.2}$$

where D_n and κ are related through (1). The DSD predicted diameter chord arrival times, or equivalently radial line arrival times (due to the symmetry of the DSD model about $r = 0$), are then given by $t(r) = -z_s(r)/D_0^{\mathrm{DSD}}$. For any given d and edge-angle ϕ_e, together with any D_{CJ}, B, C_2 and C_4 defining (1), the corresponding steady detonation axial speed D_0^{DSD} is determined by integration of (A.1) with (A.2) and iteration on D_0^{DSD} until $\phi = \phi_e$ at $r = d/2$. This also gives $z_s(r)$ and $t(r)$ for the final D_0^{DSD}.

For a given set of experimental data, we quantify the fitting accuracy of the DSD model for any B, C_2 C_4, D_{CJ} and ϕ_e relative to the difference in both the diameter effect and radial line arrival time measurements. The diameter effect contribution to the merit function is a weighted average given by

$$\mathcal{M}_{DE} = \frac{1}{\alpha_T}\sum_{i=1}^{N_{DE}}\alpha_i\left(\frac{D_{0,i}^{\mathrm{DSD}} - D_{0,i}^{\mathrm{exp}}}{\Delta D_0^{\mathrm{ref}}}\right)^2, \tag{A.3}$$

where N_{DE} is the total number of diameter effect measurements in the data set for a given lot, $\alpha_T = \sum_{i=1}^{N_{DE}}\alpha_i$ where α_i are weighting parameters, $D_{0,i}^{\mathrm{DSD}}$ is the calculated axial detonation speed obtained from the DSD model for a given experimental charge size, $D_{0,i}^{\mathrm{exp}}$ is the corresponding experimentally measured axial detonation speed, and $\Delta D_0^{\mathrm{ref}}$ is a characteristic axial speed difference. The weighting parameters and characteristic axial speed difference are

$$\alpha_i = 1/N_{d,i},\quad \Delta D_0^{\mathrm{ref}} = 0.01\ \mathrm{mm}/\mu\mathrm{s}, \tag{A.4}$$

where $N_{d,i}$ is the number of experimental shots at nominal target diameter d for a given lot.

The radial line arrival time contribution to the merit function is again a weighted average given by

$$\mathcal{M}_{AT} = \frac{1}{\beta_T}\sum_{i=1}^{N_{AT}}\left[\frac{\beta_i}{N_t^i}\sum_{j=1}^{N_t^i}\left(\frac{t_{i,j}^{\mathrm{DSD}}[r_{i,j}^{\mathrm{exp}}] - t_{i,j}^{\mathrm{exp}}}{\Delta t^{\mathrm{ref}}}\right)^2\right], \tag{A.5}$$

where N_{AT} is the total number of radial line arrival time measurements in the data set for a given lot, $\beta_T = \sum_{i=1}^{N_{AT}}\beta_i$ where β_i are weighting parameters, N_t^i is the total number of extracted data points along a radial line, $t_{i,j}^{\mathrm{exp}}$ is the experimentally measured arrival time at the extracted radial position $r_{i,j}^{\mathrm{exp}}$, $t_{i,j}^{\mathrm{DSD}}$ is the DSD calculated arrival time at $r_{i,j}^{\mathrm{exp}}$, and Δt^{ref} is a characteristic arrival time difference. The weighting parameters and characteristic arrival time difference are

$$\beta_i = \hat{\beta}_i/L_{d,i},\quad \Delta t^{\mathrm{ref}} = 0.002\ \mu\mathrm{s}, \tag{A.6}$$

where $L_{d,i}$ is the number of radial line arrival time measurements at nominal diameter d for a given lot, $\hat{\beta}_i = 10$

for the largest diameter shot available for a given lot, and $\hat{\beta}_i = 1$ otherwise. These choices of $\hat{\beta}_i$ give a higher weighting to the largest diameter test for each lot, i.e. to the one that spans the largest range of curvatures accessed in the calibration.

The combined merit function $\mathcal{M}$ is a weighted average of $\mathcal{M}_{DE}$ and $\mathcal{M}_{AT}$ given by

$$\mathcal{M} = \frac{\omega_{DE}\mathcal{M}_{DE} + \omega_{AT}\mathcal{M}_{AT}}{\omega_{DE} + \omega_{AT}}, \tag{A.7}$$

where ω_{DE} and ω_{AT} are weighting parameters. Here, $\omega_{DE} = 1$ and $\omega_{AT} = 1$, so that the diameter effect and radial line arrival time contributions have equal weighting in the merit function. Note that the characteristic difference choices ΔD_0^{ref} and Δt^{ref} were chosen so that $\mathcal{M}_{DE}$ and $\mathcal{M}_{AT}$ are $O(1)$ at the end of the Nelder-Mead minimization process, and thus by default $\mathcal{M} = O(1)$.

Also, as described in [18], since D_{CJ} and ϕ_e are not overly constraining on the DSD model fits provided they are within physically reasonable values, the optimal method of calibrating the DSD model parameters is to fix both D_{CJ} and ϕ_e and iterate only on B, C_2 and C_4. Several such minimizations are then conducted across a range of D_{CJ} and ϕ_e values and the overall lowest merit function selected. For each of the five PBX 9502 lots, we encountered only minor variations in the combined merit function for a range of D_{CJ} and ϕ_e around $D_{CJ} = 7.8$ mm/μs and $\phi_e = 30.0°$, and thus these values were selected for each PBX 9502 lot. Moreover, the choice of a single value of D_{CJ} is consistent with the CYLEX analysis presented in §4, where the heats of detonation for the five PBX 9502 lots are found to be similar.

Appendix B. JWL EOS Model Calibration Methodology

The initial starting point for the JWL product EOS parameters A, B, R_1, R_2 and ω is obtained from the analytical scaling theory developed by Jackson [21], where we use D_{CJ} for the detonation speed in place of the experimentally measured speed. The CYLEX hydrodynamic simulation (§4) outputs the predicted Cu wall radial velocity profile (u^{sim}), which is then compared to the averaged profile of the experimentally measured PDV profiles (u^{exp}) [Fig. 6a]. In order to balance the fitting errors from the ringing and smooth regions of the profile, we partition the wall velocity profile into N regions in time, with the n^{th} region denoted by Ω_n and J_n representing the total number of experimental data points within Ω_n. For the n^{th} region, the corresponding merit function is defined as a normalized root mean square of the velocity difference given by

$$\mathcal{M}_n = \left[\frac{1}{J_n}\sum_{j\in\Omega_n}\left(\frac{u^{\text{sim}}[t_j^{\text{exp}}] - u_j^{\text{exp}}}{\Delta u^{\text{ref}}}\right)^2\right]^{1/2}, \tag{B.1}$$

where t_j^{exp} and u_j^{exp} are the time measurements and corresponding radial velocity from the averaged experimental PDV probes, respectively, u^{sim} is the simulated radial velocity (which is linearly interpolated to each t_j^{exp}), and Δu^{ref} is a characteristic reference velocity difference, defined below. The combined merit function $\mathcal{M}$ is a weighted average of all $\mathcal{M}_n$ given by

$$\mathcal{M} = \frac{1}{\gamma_T}\sum_{n=1}^{N}\gamma_n M_n, \tag{B.2}$$

where γ_n is the weighting factor for the n^{th} region and $\gamma_T = \sum_{n=1}^{N}\gamma_n$. For the five lots examined, we partition the expansion profiles into two regions given by

$$\Omega_1 = \{j : 0 \le t_j^{\text{sim}} < 10\}, \quad \Omega_2 = \{j : 10 \le t_j^{\text{sim}} < t^{\max}\}, \tag{B.3}$$

where $t^{\max} = 25.0$ for lots 001-V and 008-V, while $t^{\max} = 21.0$ for lot 002-V, $t^{\max} = 23.0$ for lot 007-R and $t^{\max} = 20.0$ for lot 136-R. Also, $\gamma_1 = 1$ and $\gamma_2 = 5$, which ensures that the smooth regions of the wall expansion are captured accurately by the fitting process as desired [Fig. 21]. Finally, we set $\Delta u^{\text{ref}} = 0.02$ mm/μs, so that at the end of the Nelder-Mead minimization process, $\mathcal{M} = O(1)$.

Appendix C. Velocity-Adjusted JWL Method

The velocity-adjusted JWL method [6, 18, 19, 31] accounts for variations in the programmed burn (PB) energy release due to detonation front curvature. For JWL product EOS parameters A, B, R_1, R_2 and ω, the heat of detonation e_0 is set to ensure that the D_{CJ} associated with the PB energy release model is consistent with the value used in the DSD timing model (in this study, $D_{CJ} = 7.8$ mm/μs as described in §3). Through the CJ detonation Rayleigh line relation, we have

$$p_{CJ} = \frac{D_{CJ}^2}{v_0^2}(v_0 - v_{CJ}), \tag{C.1}$$

while C, the label for the principal isentrope, is

$$C = \left(\frac{v_{CJ}}{v_0}\right)^{1+\omega} \left(\frac{D_{CJ}^2}{v_0^2}(v_0 - v_{CJ}) - A \exp\left[-R_1 v_{CJ}/v_0\right] - B \exp\left[-R_2 v_{CJ}/v_0\right] \right). \tag{C.2}$$

Additionally, Eqn. (6) gives

$$e_0 = \frac{A v_0}{R_1} \exp\left[-R_1 v_{CJ}/v_0\right] + \frac{B v_0}{R_2} \exp\left[-R_2 v_{CJ}/v_0\right] + \frac{C v_0}{\omega}\left(\frac{v_0}{v_{CJ}}\right)^{\omega} - \frac{D_{CJ}^2}{2v_0^2}(v_0 - v_{CJ})^2, \tag{C.3}$$

while the tangency of the Rayleigh line and principal isentrope at the CJ point gives

$$\frac{A R_1}{v_0} \exp\left[-R_1 v_{CJ}/v_0\right] + \frac{B R_2}{v_0} \exp\left[-R_2 v_{CJ}/v_0\right] + \frac{(1+\omega)C}{v_{CJ}}\left(\frac{v_0}{v_{CJ}}\right)^{1+\omega} = \frac{D_{CJ}^2}{v_0^2}. \tag{C.4}$$

With $D_{CJ} = 7.8$ mm/μs, equations (C.3) and (C.4) are then solved to yield e_0 and v_{CJ}.

Along the detonation front in the DSD model, the surface normal detonation speed D_n varies with curvature κ (§3). In order to account for the energy release modification due to this variation, for any D_n on the DSD surface, we replace D_{CJ} in (C.2)-(C.4) by that D_n. Essentially, we assume that there is a one-dimensional averaged CJ detonation approximation to the curved DDZ structure present for $D_0 < D_{CJ}$. It is an approximation used in the analytical JWL EOS scaling studies of Jackson [21], and also in recent studies on the analysis of unstable gas-phase detonation propagation, where cellular waves are replaced by 1D averaged CJ structures [35–37]. The parameters A and R_1 in the high-pressure section of the JWL EOS are then modified by solution of (C.2)-(C.4) for the specified D_n. A corresponding value of $v_{CJ}(D_n)$ is also calculated. Different A and R_1 arise for different D_n, and are subsequently advected with the fluid in CYLEX hydrodynamic simulations. The values of A and R_1 reported in table 9 are those for the principal JWL EOS isentrope, i.e. for $D_n = D_{CJ}$. By varying only A and R_1, we are primarily affecting the high pressure region of the products EOS, i.e., the part of the products flow that attaches to the end of the DDZ. Thus, modification of the high pressure section of the JWL EOS allows the energy release in the PB model to synchronize with the curvature-induced influence on detonation timing through the DSD model.

References

[1] J. Dick, C. Forest, J. Ramsay, W. Seitz, The Hugoniot and shock sensitivity of a plastic-bonded TATB explosive PBX 9502, J. Appl. Phys. 63 (1988) 4881–4888.

[2] R. Gustavsen, S. Sheffield, R. Alcon, Measurements of shock initiation in the tri-amino-tri-nitro-benzene based explosive PBX 9502: Wave forms from embedded gauges and comparison of four different material lots, J. Appl. Phys. 99 (2006) 114907.

[3] M. Short, C. Chiquete, J. Bdzil, J. Quirk, Detonation diffraction in a circular arc geometry of the insensitive high explosive PBX 9502, Combust. Flame 196 (2018) 129–143.

[4] C. Tarver, Modeling detonation experiments on triaminotrinitrobenzene (TATB)-based explosives LX-17, PBX 9502, and ultrafine TATB, J. Energet. Mat. 30 (2012) 220–251.

[5] C. Hutchinson, G. Foan, H. Lawn, A. Jones, Initiation and detonation properties of the insensitive high explosive TATB/Kel-F 800 95/5, in: Ninth Symposium (International) on Detonation, Office of the Chief of Naval Research, OCNR 113291-7, 1989, pp. 123–132.

[6] A. Hodgson, C. Handley, DSD/WBL-consistent JWL equations of state for EDC35, in: AIP Conference Proceedings, volume 1426, American Institute of Physics, 2012, pp. 247–250.

[7] D. Dattelbaum, L. Stevens, Equations of state of binders and related polymers, in: Static Compression of Energetic Materials, Springer, 2009, pp. 127–202.

[8] M. Hoffman, T. Willey, A. Mitchell, S. Depiero, Comparison of new and legacy TATBs, J. Energet. Mat. 26 (2008) 139–162.

[9] J. Morris, C. Robinson, T. Mahoney, Reclamation and reformation of TATB from PBX 9502 and LX-17, Presentated at Insensitive Munitions and Energetics Materials Symposium, San Diego, CA., 2013.

[10] B. Dobratz, The insensitive high explosive triaminotrinitrobenzene (TATB): Development and characterization, 1888 to 1994, Technical Report LA-13014-H, Los Alamos National Lab., NM (United States), 1995.

[11] L. Hill, J. Bdzil, W. Davis, R. Critchfield, PBX 9502 front curvature ratestick data: repeatability and the effects of temperature and material variation, in: Thirteenth International Detonation Symposium, Office of Naval Research, ONR 351-07-01, 2006, pp. 331–341.

[12] P. Peterson, D. Idar, Microstructural differences between virgin and recycled lots of PBX 9502, Propell. Explos. Pyrotech 30 (2005) 88–94.

[13] W. Seitz, Short-duration shock initiation of triaminotrinitrobenzene (TATB), in: Shock Waves in Condensed Matter 1983, Elsevier, 1984, pp. 531–534.

[14] R. Gustavsen, R. Gehr, S. Bucholtz, R. Alcon, B. Bartram, Shock initiation of the tri-amino-tri-nitro-benzene based explosive PBX 9502 cooled to -55 °C, J. Appl. Phys. 112 (2012) 074909.

[15] L. Hill, T. Aslam, Detonation shock dynamics calibration for PBX 9502 with temperature, density, and material lot variations, in: Fourteenth International Detonation Symposium, Office of Naval Research, ONR-351-10-185, 2010, pp. 779–788.

[16] M. Short, J. Quirk, High explosive detonation-confiner interactions, Annu. Rev. Fluid Mech. 50 (2018) 215–242.

[17] S. Jackson, Scaled cylinder test experiments with insensitive PBX 9502 explosive, in: Thirteenth International Detonation Symposium, Office of Naval Research, ONR-43-280-15, 2014, pp. 171–180.

[18] C. Chiquete, M. Short, E. Anderson, S. Jackson, Detonation shock dynamics modeling and calibration of the HMX-based conventional high explosive PBX 9501 with application to the

two-dimensional circular arc geometry, Combust. Flame 222 (2020) 213–232.
[19] E. Anderson, C. Chiquete, S. Jackson, R. Chicas, M. Short, The comparative effect of HMX content on the detonation performance characterization of PBX 9012 and PBX 9501 high explosives, Combust. Flame 230 (2021) 111415.
[20] F. Acton, Analysis of straight-line data, Wiley New York, 1959.
[21] S. Jackson, Scaling of the detonation product state with reactant kinetic energy, Combust. Flame 190 (2018) 240–251.
[22] J. Bdzil, D. Stewart, The dynamics of detonation in explosive systems, Ann. Rev. Fluid Mech. 39 (2007) 263–292.
[23] J. Nelder, R. Mead, A simplex method for function minimization, The Computer Journal 7 (1965) 308–313.
[24] S. Jackson, M. Short, Scaling of detonation velocity in cylinder and slab geometries for ideal, insensitive and non-ideal explosives, J. Fluid Mech. 773 (2015) 224–266.
[25] M. Short, J. Quirk, C. Meyer, C. Chiquete, Steady detonation propagation in a circular arc: a Detonation Shock Dynamics model, J. Fluid Mech. 807 (2016) 87–134.
[26] E. Ioannou, S. Schoch, N. Nikiforakis, L. Michael, Detonation propagation in annular arcs of condensed phase explosives, Phys. Fluids 29 (2017) 116102.
[27] M. Short, J. Quirk, C. Chiquete, C. Meyer, Detonation propagation in a circular arc: reactive burn modelling, J. Fluid Mech. 835 (2018) 970–998.
[28] M. Short, E. Anderson, C. Chiquete, S. Jackson, Experimental and modeling analysis of detonation in circular arcs of the conventional high explosive PBX 9501, Proc. Combust. Instit. 38 (2021) 3683–3690.
[29] W. Davis, Shock waves; rarefraction waves; equations of state, in: J. Zukas, W. Walters (Eds.), Explosive Effects and Applications, Springer, 1997, pp. 47–113.
[30] D. Burton, Multidimensional discretization of conservation laws for unstructured polyhedral grids, Technical Report UCRL-JC-118306, Lawrence Livermore National Lab., CA (United States), 1994.
[31] C. Chiquete, S. Jackson, Detonation performance of the CL-20-based explosive LX-19, Proc. Combust. Instit. 38 (2021) 3661–3669.
[32] J. Peterson, K. Honnell, C. Greeff, J. Johnson, J. Boettger, S. Crockett, Global equation of state for copper, in: AIP Conference Proceedings, volume 1426, American Institute of Physics, 2012, pp. 763–766.
[33] D. Preston, D. Tonks, D. Wallace, Model of plastic deformation for extreme loading conditions, J. Appl. Phys. 93 (2003) 211–220.
[34] C. Chiquete, S. Jackson, E. Anderson, M. Short, S. Voelkel, V. Whitley, Detonation performance model calibration and validation of the HMX-based high explosive PBX 9501, Proceedings of the 28th International Colloquium on the Dynamics of Explosions and Reactive Systems, Napoli, Italy, June 19th-24th, 2022.
[35] M. Radulescu, G. Sharpe, C. Law, J. Lee, The hydrodynamic structure of unstable cellular detonations, J. Fluid Mech. 580 (2007) 31–81.
[36] M. Radulescu, A detonation paradox: Why inviscid detonation simulations predict the incorrect trend for the role of instability in gaseous cellular detonations?, Combust. Flame 195 (2018) 151–162.
[37] M. Reynaud, S. Taileb, A. Chinnayya, Computation of the mean hydrodynamic structure of gaseous detonations with losses, Shock Waves 30 (2020) 645–669.